JOHANNES-GUTENBERG-UNIVERSITÄT MAINZ
INSTITUT FÜR PHYSIK

Time Scaling in Coarse-Graining Mappings

Diplomarbeit

verfasst und vorgelegt von

Konstantin Koschke

angefertigt am Max-Planck-Institut für Polymerforschung

Mainz, Dezember 2009

Contents

Contents

Introduction and Motivation

Coarse-graining stands for replacing a detailed (fine-grained) description with a lower resolution (coarse-grained) model by reducing the amount of degrees of freedom through averaging or smoothing out. Correspondingly small scale motions in the fine grained model are not resolved on the coarse scale and thus, these different length scales correspond to different characteristic time scales. While the length scaling is obvious, the link between different time scales is not. Of special interest is the a priori knowledge about the time scaling behavior while linking one description to another.

Computer simulations in physics are widely used to gain a better understanding of various systems. One particular simulation method, Molecular Dynamics, allows one to investigate physics and its applications in, e.g., chemistry starting from the macroscopic down to the atomistic scale hitting the limits of classical mechanics. Choosing the right resolution, dependent upon the questions one is engaged in, can be the key task to success while looking for answers.

Molecular Dynamics and its variations contain time as an explicit variable and dynamic properties, for instance, conformational changes, are directly accessible. The main idea in any Molecular Dynamics algorithm is solving the discretized and therefore approximated equations of motion for a small timestep. Here, the physical and chemical task is the right set-up of the model, especially the correct definition of potentials and forces involved, whereas the computational task is the efficient calculation of these forces and integration of the equations of motion.

Different models for the same system not only point out different properties, but also influence the computer time needed for a simulation run. Coarse-grained models have two advantages: the computational part is accelerated, resulting in accessible time and length that are far beyond atomistic simulations, and unneccessary details are ignored. Both are consequences of a reduced set of degrees of freedom. E.g.,

1. an atomistic model of a polymer contains all atoms which are present in the real polymer. Furthermore, their interactions are modelled as completeley as possible and are summed up as mathematical functions and parameters into so-called force-fields. The enormous number of force-fields[1] illustrates the complexity of this task.

2. A coarse-grained model of the same polymer simplifies its representation by introducing beads, which consist of a group of atoms, e.g. monomers, parts of

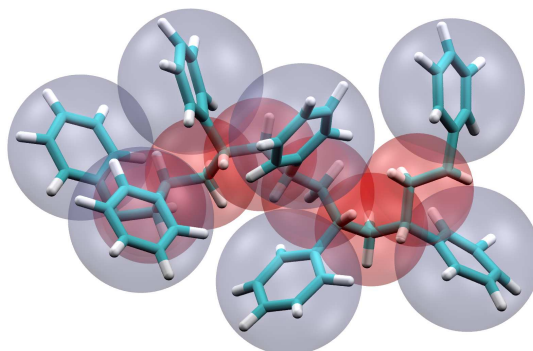monomers or even parts of atoms (see figure A). Effective interactions are used only between these beads.

Figure A: Polystyrene C_8H_8. The spheres indicate the grouping of atoms. This picture is taken from reference [2].

A coarse-grained model will reproduce certain features of the atomistic model. Often, it will also allow one to reobtain the atomistic resolution by applying a reverse, non-bijective mapping, called back-mapping. However, the other side of the coin is usually a loss of accuracy by giving up certain degrees of freedom.

Accuracy is also an issue in every atomistic model. All models are approximations themselves; most are based on experimental data and calculations from quantum chemistry.

The aim of this work is to systematically investigate the time scaling behavior of coarse-graining mappings. Also, possibilites and limits of predictions for the time speed-up are shown. Chapter 1 gives the theoretical background of a supposedly simple system and its description by the Langevin equation of motion. In chapter 2, a very general procedure for computer simulations is briefly introduced. Additional methods are combined with the general idea and applied to simple and more realistic systems. The results are collected and discussed in chapter 3.

1 Langevin Dynamics

"Time Scaling in Coarse-Graining Mappings" – a title that certainly needs some explanation.

If physical systems become too complex – realistic systems unfortunately tend to – one often has to leave an analytic description and can instead use, for instance, a numerical approach[1]. Numerical approaches introduce new and unphysical errors. Nevertheless, they allow one to characterize a system to a certain level. Computer simulations are based on numerical approaches. Their correctness is in addition limited by the computer's hardware. While setting up a model for a simulation, one has to include the parameters characterizing the real system and translate the physical behavior into a computer-friendly algorithm. Some of these algorithms solve the given equation of motion step by step – a computer time step. Before one can interpret the results, a link to the real time has to be established. This link is usually based on experiments. The simulation is then able to reproduce previous results and motivate – based on a simulation set-up that can not be realized as easily in a real lab – new experiments. However, setting up a simulation is a non-trivial task and there are many different ways to describe the very same system leading to different simulation models. Among others, one question is especially eminent: how are different (simulation) models of one system linked to *each other*? How does the time scale while switching from one description to another?

We will compare the two time scales of two different models by studying diffusive dynamics. Diffusive dynamics gives us information about the intrinsic time scale. Assuming we had two models (of the same system) resulting in two different effective potentials, we would still expect diffusive dynamics to be the same. The difference in dynamics caused by the difference in potentials would therefore require to be compensated by an adjustment of the time scale. That means, if the diffusion belonging to potential 1 and characterized by the diffusion constant D^{P1} is faster than the diffusion belonging to potential 2, i.e. $D^{P1} > D^{P2}$, we need to rescale the time t^{P1} in order to match diffusive dynamics belonging to each potential. Since we know from Einstein's equation for the diffusion constant that $D \propto 1/\text{time}$, the ratio of D^{P1} and D^{P2} gives us the scaling factor. In other words, if we could calculate the diffusion constant for any given potential, we would be able to predict the link between the time scales of different potentials. Thus, the calculation of the diffusion constant is

---

[1] Analytic approaches themselves are approximated models of the real world.

our main task. We start with a simple system.

1.1 Langevin and Kramers Equation

The Langevin equation describes the Brownian motion of one particle with mass m in a potential $U(x)$ and reads

$$m\ddot{x} = -\frac{\mathrm{d}}{\mathrm{d}x}U(x) - \gamma m\dot{x} + \xi(t), \tag{1.1}$$

where γ is the constant friction and $\xi(t)$ the Gaussian white noise fulfilling the fluctuation-dissipation theorem ($k_B T$ is the Boltzmann constant multiplied by the temperature)

$$\langle \xi(t) \rangle = 0,$$

$$\langle \xi(t)\xi(s) \rangle = 2m\gamma k_B T \delta(t-s).$$

The equivalent[3, p. 72] Klein-Kramers equation, a special case of the more general Fokker-Planck equation (FPE), describes the time evolution of the probability density $\rho(x,v,t)$ for the coordinate x and velocity $v = \dot{x}$,

$$\frac{\partial}{\partial t}\rho(x,v,t) = \left[-\frac{\partial}{\partial x}v + \frac{\partial}{\partial v}\left(\frac{1}{m}\frac{\mathrm{d}}{\mathrm{d}x}U(x) + \gamma v \right) + \gamma v_{\mathrm{th}}^2 \frac{\partial^2}{\partial v^2} \right]\rho(x,v,t). \tag{1.2}$$

Using the Fokker-Planck operator $\mathbf{L_K}$, equation (1.2) reads

$$\frac{\partial}{\partial t}\rho = \mathbf{L_K}\rho, \tag{1.3}$$

where $\mathbf{L_K}$ can be split into an irreversible and reversible part[3, p. 231]

$$\mathbf{L_K} = \mathbf{L_{ir}} + \mathbf{L_{rev}}, \tag{1.4}$$

$$\mathbf{L_{ir}} = \gamma\frac{\partial}{\partial v}\left(v + v_{\mathrm{th}}^2\frac{\partial}{\partial v} \right), \tag{1.5}$$

$$\mathbf{L_{rev}} = -v\frac{\partial}{\partial x} + \frac{1}{m}\frac{\mathrm{d}U}{\mathrm{d}x}\frac{\partial}{\partial v}, \tag{1.6}$$

with the thermal velocity $v_{\mathrm{th}}^2 = k_B T/m$. We multiply $\mathbf{L_{ir}}$ from the right with the square root of the stationary solution, $\exp\left[-v^2/(2v_{\mathrm{th}}^2)\right]$, and from the left with the inverse of the square root of the stationary solution, in order to bring $\mathbf{L_{ir}}$ to an hermitian form (we include the mass m in our potential and redefine $U(x)$,

$$m\tilde{U}(x) = U(x) \Rightarrow \tilde{U}(x) = U(x)/m =: U(x))$$

$$\bar{\mathbf{L}}_{\mathrm{ir}} = e^{\frac{1}{4}v^2/v_{\mathrm{th}}^2}\mathbf{L}_{\mathrm{ir}}\, e^{-\frac{1}{4}v^2/v_{\mathrm{th}}^2} \tag{1.7}$$

$$= \gamma e^{\frac{1}{4}v^2/v_{\mathrm{th}}^2}\left(\frac{\partial}{\partial v}v + v_{\mathrm{th}}^2\frac{\partial^2}{\partial v^2}\right)e^{-\frac{1}{4}v^2/v_{\mathrm{th}}^2}$$

$$= \gamma e^{\frac{1}{4}v^2/v_{\mathrm{th}}^2}\, e^{-\frac{1}{4}v^2/v_{\mathrm{th}}^2}$$

$$\times\left(1 - \frac{1}{2}\frac{v^2}{v_{\mathrm{th}}^2} + v\frac{\partial}{\partial v} + \frac{1}{4}\frac{v^2}{v_{\mathrm{th}}^2} - v\frac{\partial}{\partial v} - \frac{1}{2} + v_{\mathrm{th}}^2\frac{\partial^2}{\partial v^2}\right)$$

$$= \gamma\left(\frac{1}{2} - \frac{1}{4}\frac{v^2}{v_{\mathrm{th}}^2} + v_{\mathrm{th}}^2\frac{\partial^2}{\partial v^2}\right)$$

$$\Rightarrow \bar{\mathbf{L}}_{\mathrm{ir}} = \gamma\left(\frac{1}{2} - \frac{1}{4}\frac{v^2}{v_{\mathrm{th}}^2} + v_{\mathrm{th}}^2\frac{\partial^2}{\partial v^2}\right) = \bar{\mathbf{L}}_{\mathrm{ir}}^+. \tag{1.8}$$

$\bar{\mathbf{L}}_{\mathrm{ir}}^+$ is the hermitian adjoint of $\bar{\mathbf{L}}_{\mathrm{ir}}$. The obvious analogy with the Hamilton operator for the harmonic oscillator in quantum mechanics is used and we introduce the creation and annihilation operators b^+ and b,

$$b = v_{\mathrm{th}}\frac{\partial}{\partial v} + \frac{1}{2}\frac{v}{v_{\mathrm{th}}}, \qquad\qquad b^+ = -v_{\mathrm{th}}\frac{\partial}{\partial v} + \frac{1}{2}\frac{v}{v_{\mathrm{th}}},$$

$$[b, b^+] = 1,$$

where the brackets denote the commutator for these boson operators. $\bar{\mathbf{L}}_{\mathrm{ir}}$ can be now written as

$$\bar{\mathbf{L}}_{\mathrm{ir}} = -\gamma b^+ b \tag{1.9}$$

and motivates the transformation of the reversible part as well. However, we choose a more general transformation[3, p. 233]:

$$\bar{\mathbf{L}}_{\mathrm{K}} = \bar{\mathbf{L}}_{\mathrm{rev}} + \bar{\mathbf{L}}_{\mathrm{ir}} \tag{1.10}$$

$$\bar{\mathbf{L}}_{\mathrm{ir,rev}} = \exp\left[\frac{1}{4}\frac{v^2}{v_{\mathrm{th}}^2} + \frac{1}{2}\frac{U(x)}{v_{\mathrm{th}}^2}\right]\mathbf{L}_{\mathrm{ir,rev}}\exp\left[-\frac{1}{4}\frac{v^2}{v_{\mathrm{th}}^2} - \frac{1}{2}\frac{U(x)}{v_{\mathrm{th}}^2}\right]. \tag{1.11}$$

Since $\mathbf{L}_{ir}$ does not act on x, $\bar{\mathbf{L}}_{ir}$ is still given by equation (1.9). $\bar{\mathbf{L}}_{rev}$ is obtained to

$$
\begin{aligned}
\bar{\mathbf{L}}_{rev} &= \exp\left[\frac{1}{4}\frac{v^2}{v_{th}^2} + \frac{1}{2}\frac{U(x)}{v_{th}^2}\right]\left(-v\frac{\partial}{\partial x} + \frac{dU}{dx}\frac{\partial}{\partial v}\right)\exp\left[-\frac{1}{4}\frac{v^2}{v_{th}^2} - \frac{1}{2}\frac{U(x)}{v_{th}^2}\right] \quad (1.12) \\
&= \exp\left[\frac{1}{4}\frac{v^2}{v_{th}^2} + \frac{1}{2}\frac{U(x)}{v_{th}^2}\right]\exp\left[-\frac{1}{4}\frac{v^2}{v_{th}^2} - \frac{1}{2}\frac{U(x)}{v_{th}^2}\right] \\
&\quad \times \left(\frac{1}{2}\frac{v}{v_{th}^2}\frac{dU}{dx} - v\frac{\partial}{\partial x} - \frac{1}{2}\frac{v}{v_{th}^2}\frac{dU}{dx} + \frac{dU}{dx}\frac{\partial}{\partial v}\right) \\
&= -v\frac{\partial}{\partial x} + \frac{dU}{dx}\frac{\partial}{\partial v} \\
&= \mathbf{L}_{rev}. \quad (1.13)
\end{aligned}
$$

We introduce the differential operators D and $\hat{D}$

$$
D = v_{th}\frac{\partial}{\partial x} - \frac{1}{2v_{th}}\frac{dU}{dx}, \qquad\qquad \hat{D} = v_{th}\frac{\partial}{\partial x} + \frac{1}{2v_{th}}\frac{dU}{dx},
$$

$$
[D, \hat{D}] = \frac{d^2U}{dx^2} \quad\text{and}\qquad\qquad D^+ = -v_{th}\frac{\partial}{\partial x} - \frac{1}{2v_{th}}\frac{dU}{dx} = -\hat{D}.
$$

This gives us

$$
\bar{\mathbf{L}}_{rev} = -bD - b^+\hat{D},
$$
$$
\bar{\mathbf{L}}_{rev}^+ = -b^+D^+ - b\hat{D}^+ = b^+\hat{D} + bD = -\bar{\mathbf{L}}_{rev}
$$

and $\bar{\mathbf{L}}_K$ becomes

$$
\bar{\mathbf{L}}_K = -bD - b^+\hat{D} - \gamma b^+ b. \quad (1.14)
$$

The velocity part of $\rho(x, v, t)$ can be expanded into Hermite functions. These are the eigenfunctions of $\bar{\mathbf{L}}_{ir} = -\gamma b^+ b$,

$$
\bar{\mathbf{L}}_{ir}\psi_n(v) = -\gamma n \psi_n(v), \quad (1.15)
$$

and are given by

$$
\psi_n(v) = \frac{(b^+)^n}{\sqrt{n!}}\,\psi_0(v), \quad (1.16)
$$

$$
\psi_0(v) = \frac{e^{-\frac{1}{4}v^2/v_{th}^2}}{\sqrt[4]{2\pi v_{th}^2}}, \quad (1.17)
$$

or in terms of Hermite polynomials $H_n(x)$,

$$\psi_n(v) = H_n\left(v/\sqrt{2}v_{\text{th}}\right) \frac{e^{-\frac{1}{4}v^2/v_{\text{th}}^2}}{\sqrt{n!2^n v_{\text{th}}\sqrt{2\pi}}}. \tag{1.18}$$

After artificially rewriting $\mathbf{L_K}$,

$$\mathbf{L_K} = \overline{\mathbf{L_K}},$$

$$\mathbf{L_K} = \exp\left[-\frac{1}{4}\frac{v^2}{v_{\text{th}}^2} - \frac{1}{2}\frac{U(x)}{v_{\text{th}}^2}\right] \bar{\mathbf{L}}_K \exp\left[+\frac{1}{4}\frac{v^2}{v_{\text{th}}^2} + \frac{1}{2}\frac{U(x)}{v_{\text{th}}^2}\right],$$

$$= \exp\left[-\frac{1}{4}\frac{v^2}{v_{\text{th}}^2} - \frac{1}{2}\frac{U(x)}{v_{\text{th}}^2}\right]\left(-bD - b^+\hat{D} - \gamma b^+ b\right)\exp\left[+\frac{1}{4}\frac{v^2}{v_{\text{th}}^2} + \frac{1}{2}\frac{U(x)}{v_{\text{th}}^2}\right],$$

$$= -\psi_0(v)\, e^{-\frac{1}{2}U(x)/v_{\text{th}}^2}\left(bD + b^+\hat{D} + \gamma b^+ b\right)\psi_0^{-1}(v)\, e^{\frac{1}{2}U(x)/v_{\text{th}}^2}, \tag{1.19}$$

where we used equation (1.17) in the last step, the form of $\mathbf{L_K}$ suggests to expand $\rho(x, v, t)$ as follows:

$$\rho(x, v, t) = \psi_0(v)\, e^{-\frac{1}{2}U(x)/v_{\text{th}}^2} \sum_{n=0}^{\infty} c_n(x, t)\psi_n(v). \tag{1.20}$$

We have transformed the problem of solving equation (1.2) to finding the expansion coefficients $c_n(x, t)$. By inserting equation (1.20) into the Fokker-Planck equation (1.2), we obtain an equation of motion for those coefficients:

$$\frac{\partial}{\partial t}\rho(x, v, t) = -\psi_0(v)\, e^{-\frac{1}{2}U(x)/v_{\text{th}}^2}\left(bD + b^+\hat{D} + \gamma b^+ b\right)\psi_0^{-1}(v)\, e^{\frac{1}{2}U(x)/v_{\text{th}}^2}\rho(x, v, t) \tag{1.21}$$

$$\Leftrightarrow \sum_{n=0}^{\infty} \dot{c}_n(x, t)\psi_n(v) = -\left(bD + b^+\hat{D} + \gamma b^+ b\right)\sum_{n=0}^{\infty} c_n(x, t)\psi_n(v) \tag{1.22}$$

- $\gamma b^+ b \sum_{n=0}^{\infty} c_n(x, t)\psi_n(v) = n\sum_{n=0}^{\infty} \gamma c_n(x, t)\psi_n(v)$

- $b^+\hat{D} \sum_{n=0}^{\infty} c_n(x, t)\psi_n(v) = \sum_{n=0}^{\infty} \hat{D}c_n(x, t)\sqrt{n+1}\psi_{n+1}(v)$

- $bD \sum_{n=0}^{\infty} c_n(x, t)\psi_n(v) = \sum_{n=0}^{\infty} Dc_n(x, t)\sqrt{n}\psi_{n-1}(v)$

$$\Leftrightarrow \sum_{n=0}^{\infty} \dot{c}_n(x,t)\psi_n(v) = -\sum_{n=0}^{\infty}\left[Dc_n(x,t)\sqrt{n}\psi_{n-1}(v)\right.$$

$$+ \hat{D}c_n(x,t)\sqrt{n+1}\psi_{n+1}(v)$$

$$\left.+ \gamma n c_n(x,t)\psi_n(v)\right] \tag{1.23}$$

$$\bullet \quad c_n(x,t)\sqrt{n}\psi_{n-1}(v) \xrightarrow{n\to n-1} c_{n+1}(x,t)\sqrt{n+1}\psi_n(v)$$

$$\bullet \quad c_n(x,t)\sqrt{n+1}\psi_{n+1}(v) \xrightarrow{n\to n+1} c_{n-1}(x,t)\sqrt{n}\psi_n(v)$$

$$\Leftrightarrow \sum_{n=0}^{\infty} \dot{c}_n(x,t)\psi_n(v) = -\sum_{n=0}^{\infty}\left[Dc_{n+1}(x,t)\sqrt{n+1}\right.$$

$$+ \hat{D}c_{n-1}(x,t)\sqrt{n}$$

$$\left.+ \gamma c_n(x,t)n\right]\psi_n(v) \tag{1.24}$$

We obtain

$$\Rightarrow \dot{c}_n(x,t) = -\sqrt{n}\hat{D}c_{n-1}(x,t) - n\gamma c_n(x,t) - \sqrt{n+1}Dc_{n+1}(x,t) \tag{1.25}$$

with $c_n(x,t) = 0$ for $n \leq 0$. This tridiagonal coupled system has in general no exact solution. A numerical approach is applied to periodic potentials[3, p. 249]. Nevertheless, the steps made are also useful for further analytical studies.

The result in equation (1.25) was obtained by transforming the Fokker-Planck operator in order to use Hilbert space methods. The particular transformation in equation (1.11) is based on the stationary solution and reads more generally

$$\bar{\mathbf{L}}_{\text{ir,rev}} = \exp\left[\frac{1}{4}\frac{v^2}{v_{\text{th}}^2} + \varepsilon\frac{U(x)}{v_{\text{th}}^2}\right]\mathbf{L}_{\text{ir,rev}}\exp\left[-\frac{1}{4}\frac{v^2}{v_{\text{th}}^2} - \varepsilon\frac{U(x)}{v_{\text{th}}^2}\right]. \tag{1.26}$$

Nevertheless, analogous calculations and

$$D = v_{\text{th}}\frac{\partial}{\partial x} - \frac{\varepsilon}{v_{\text{th}}}\frac{\mathrm{d}U}{\mathrm{d}x}, \qquad \hat{D} = v_{\text{th}}\frac{\partial}{\partial x} + \frac{1-\varepsilon}{v_{\text{th}}}\frac{\mathrm{d}U}{\mathrm{d}x}, \tag{1.27}$$

will lead to equation (1.25) as well[3]. While we have used $\varepsilon = \frac{1}{2}$ in our above calculations, other values for ε may be suited better depending on the specific question.

Nuclear magnetic resonance studies have shown, that for dense polymers the ballistic part is damped out on a very short time range. This implies a large friction constant. Thus, we now consider the high friction limit of equation (1.1).

1.2 Smoluchowski Limit

For the special case of a large friction constant, one may neglect the inertia term in equation (1.1). The derivation of the corresponding Fokker-Planck equation for the Langevin equation

$$\gamma \dot{x} + \frac{dU}{dx} = \xi(t) \tag{1.28}$$

follows (still considering the potential as $mU(x)$).

We use equation (1.25) to obtain

$$
\begin{aligned}
n = 0: \quad & \dot{c}_0 = -Dc_1 \\
n = 1: \quad & \dot{c}_1 = -\hat{D}c_0 - \gamma c_1 - \sqrt{2}Dc_2 \\
n = 2: \quad & \dot{c}_2 = -\sqrt{2}\hat{D}c_1 - 2\gamma c_2 - \sqrt{3}Dc_3 \\
\cdots \quad & \cdots
\end{aligned}
$$

and truncate this system after the second term, i.e. $c_2 = c_3 = \cdots = 0$. In

$$\frac{\partial}{\partial t} c_0 + Dc_1 = 0 \quad \text{and} \tag{1.29}$$

$$\frac{\partial}{\partial t} c_1 + \hat{D}c_0 + \gamma c_1 = 0 \tag{1.30}$$

we furthermore neglect the time derivative $\partial c_1 / \partial t$ for large friction constants. With

$$D = v_{\text{th}} \frac{\partial}{\partial x} \quad \text{and} \quad \hat{D} = v_{\text{th}} \frac{\partial}{\partial x} + \frac{1}{v_{\text{th}}} \frac{dU}{dx}, \tag{1.31}$$

($\varepsilon = 0$ in equation (1.27)) equations (1.29) and (1.30) lead to

$$\frac{\partial}{\partial t} c_0 = \frac{1}{\gamma} \frac{\partial}{\partial x} \left(v_{\text{th}}^2 \frac{\partial}{\partial x} + \frac{dU}{dx} \right) c_0, \tag{1.32}$$

where

$$c_0(x, t) = \int dv\, \rho(x, v, t) = \rho(x, t) \tag{1.33}$$

is the distribution in position only[3]. Equation (1.32) is the Smoluchowski equation and describes the one-dimensional Brownian motion of a particle in the potential $mU(x)$ for the high-friction limit.

We concentrate on the stationary case $\rho(x, t) \equiv \rho(x)$,

$$0 = \frac{\partial}{\partial t} \rho(x) = \frac{1}{\gamma} \frac{\partial}{\partial x} \left(\frac{dU}{dx} + v_{\text{th}}^2 \frac{\partial}{\partial x} \right) \rho(x) = -\frac{\partial}{\partial x} S, \tag{1.34}$$

where we have introduced[3, p. 287] the constant probability current S,

$$\gamma S = -\left(\frac{\mathrm{d}U}{\mathrm{d}x} + v_{\mathrm{th}}^2 \frac{\partial}{\partial x}\right)\rho(x). \tag{1.35}$$

The solution of equation (1.34)[3, p. 288] with N as a normalization constant reads

$$\rho(x) = e^{-U(x)/v_{\mathrm{th}}^2}\left[N - \gamma\frac{S}{v_{\mathrm{th}}^2}\int_0^x \mathrm{d}x'\, e^{U(x')/v_{\mathrm{th}}^2}\right]. \tag{1.36}$$

We add a constant force F to our system and replace $U(x)$ by the total potential $\phi(x) = U(x) - Fx$. We will later take the limit of $F \to 0$ and apply the result to a 2π-periodic potential. We therefore expect $\rho(x)$ to be 2π-periodic as well. The proof follows: $(0 \le x < 2\pi)$

$$\int_0^{2\pi n+x} \mathrm{d}x'\, e^{\phi(x')/v_{\mathrm{th}}^2} = \int_0^{2\pi} \mathrm{d}x'\, e^{\phi(x')/v_{\mathrm{th}}^2} + \cdots + \int_{2\pi(n-1)}^{2\pi n} \mathrm{d}x'\, e^{\phi(x')/v_{\mathrm{th}}^2} + \int_{2\pi n}^{2\pi n+x} \mathrm{d}x'\, e^{\phi(x')/v_{\mathrm{th}}^2} \tag{1.37}$$

We make use of the following relations and definitions

- $\phi(2\pi n + x') = U(x') - (2\pi n + x')F = \phi(x') - 2\pi nF,$

- $\displaystyle\int_{2\pi(n-1)}^{2\pi n} \mathrm{d}x'\, e^{\phi(x')/v_{\mathrm{th}}^2} = \int_0^{2\pi} \mathrm{d}x'\, e^{\phi(x')/v_{\mathrm{th}}^2}\, e^{-2\pi(n-1)F/v_{\mathrm{th}}^2},$

- $\displaystyle\Omega := \int_0^{2\pi} \mathrm{d}x'\, e^{\phi(x')/v_{\mathrm{th}}^2}$

and obtain

$$\Leftrightarrow \int_0^{2\pi n+x} \mathrm{d}x'\, e^{\phi(x')/v_{\mathrm{th}}^2} = \Omega + \Omega\, e^{-2\pi F/v_{\mathrm{th}}^2} + \cdots + \Omega\, e^{-2\pi(n-1)F/v_{\mathrm{th}}^2}$$

$$+ \int_0^x \mathrm{d}x'\, e^{\phi(x')/v_{\mathrm{th}}^2}\, e^{-2\pi nF/v_{\mathrm{th}}^2}. \tag{1.38}$$

The geometric series simplifies to

$$\sum_{i=0}^{n-1} e^{-2\pi iF/v_{\mathrm{th}}^2} = \frac{1 - e^{-2\pi nF/v_{\mathrm{th}}^2}}{1 - e^{-2\pi F/v_{\mathrm{th}}^2}} \tag{1.39}$$

and equation (1.38) becomes

$$\int\limits_0^{2\pi n+x} dx'\, e^{\phi(x')/v_{th}^2} = \Omega \frac{1 - e^{-2\pi nF/v_{th}^2}}{1 - e^{-2\pi F/v_{th}^2}} + \int\limits_0^x dx'\, e^{\phi(x')/v_{th}^2}\, e^{-2\pi nF/v_{th}^2}. \tag{1.40}$$

$$\stackrel{(1.36)}{\Rightarrow} \rho(x+2\pi n) = e^{-\phi(x+2\pi n)/v_{th}^2}\left[N - \gamma\frac{S}{v_{th}^2} \int\limits_0^{2\pi n+x} dx'\, e^{\phi(x')/v_{th}^2}\right] \tag{1.41}$$

$$= e^{-\phi(x)/v_{th}^2}\, e^{2\pi nF/v_{th}^2}\left[N - \gamma\frac{S}{v_{th}^2}\left(\Omega\frac{1 - e^{-2\pi nF/v_{th}^2}}{1 - e^{-2\pi F/v_{th}^2}}\right.\right.$$

$$\left.\left. + \int\limits_0^x dx'\, e^{\phi(x')/v_{th}^2}\, e^{-2\pi nF/v_{th}^2}\right)\right] \tag{1.42}$$

$$= e^{-\phi(x)/v_{th}^2}\left[\left(N - \frac{\gamma S\Omega}{v_{th}^2(1 - e^{-2\pi F/v_{th}^2})}\right) e^{2\pi nF/v_{th}^2}\right.$$

$$\left. + \frac{\gamma S\Omega}{v_{th}^2(1 - e^{-2\pi F/v_{th}^2})} - \gamma\frac{S}{v_{th}^2}\int\limits_0^x dx'\, e^{\phi(x')/v_{th}^2}\right] \tag{1.43}$$

For $n \to \infty$ and $F > 0$ or $n \to -\infty$ and $F < 0$, the first round bracket has to vanish,

$$\Rightarrow N(1 - e^{-2\pi F/v_{th}^2}) = \gamma S\Omega/v_{th}^2. \tag{1.44}$$

Equation (1.43) becomes

$$\rho(x+2\pi n) = e^{-\phi(x)/v_{th}^2}\left[\frac{\gamma S\Omega}{v_{th}^2(1 - e^{-2\pi F/v_{th}^2})} - \gamma\frac{S}{v_{th}^2}\int\limits_0^x dx'\, e^{\phi(x')/v_{th}^2}\right],$$

$$\stackrel{(1.44)}{=} e^{-\phi(x)/v_{th}^2}\left[N - \gamma\frac{S}{v_{th}^2}\int\limits_0^x dx'\, e^{\phi(x')/v_{th}^2}\right], \tag{1.45}$$

$$\Rightarrow \rho(x+2\pi n) = \rho(x), \tag{1.46}$$

as stated above. We normalize $\rho(x)$ on its periodicity interval $0\dots 2\pi$,

$$1 \stackrel{!}{=} \int\limits_0^{2\pi} dx\, \rho(x) = N\int\limits_0^{2\pi} dx\, e^{-\phi(x)/v_{th}^2} - \gamma\frac{S}{v_{th}^2}\int\limits_0^{2\pi} dx\left[e^{-\phi(x)/v_{th}^2}\int\limits_0^x dx'\, \exp e^{\phi(x')/v_{th}^2}\right] \tag{1.47}$$

15

and obtain for the mean drift velocity $\langle v \rangle$ from equation (1.28)

$$
\begin{aligned}
\langle v \rangle &= \frac{1}{\gamma} \langle \xi(t) - \frac{\mathrm{d}}{\mathrm{d}x} \phi(x) \rangle, \\
&= \frac{1}{\gamma} \langle 0 \rangle - \frac{1}{\gamma} \langle F - \frac{\mathrm{d}U}{\mathrm{d}x} \rangle, \\
&= \frac{1}{\gamma} \int_0^{2\pi} \mathrm{d}x \left(F - \frac{\mathrm{d}U}{\mathrm{d}x} \right) \rho(x), \\
&= \frac{1}{\gamma} \int_0^{2\pi} \mathrm{d}x \left(\gamma S + v_{\mathrm{th}}^2 \frac{\partial}{\partial x} \rho(x) \right), \quad \text{with } S = \text{const.}, \\
&= 2\pi S,
\end{aligned}
$$

where we used equations (1.35), (1.46). N and S are replaced by combining equation (1.44) with (1.47) and it follows

$$
\gamma \langle v \rangle = 2\pi \gamma S = 2\pi \gamma \frac{N v_{\mathrm{th}}^2 (1 - e^{-2\pi F/v_{\mathrm{th}}^2})}{\gamma \int_0^{2\pi} \mathrm{d}x \, e^{\phi(x)/v_{\mathrm{th}}^2}}, \tag{1.48}
$$

$$
= 2\pi v_{\mathrm{th}}^2 \frac{1 - e^{-2\pi F/v_{\mathrm{th}}^2}}{\int_0^{2\pi} \mathrm{d}x \, e^{\phi(x)/v_{\mathrm{th}}^2}} \left[\int_0^{2\pi} \mathrm{d}x \, e^{-\phi(x)/v_{\mathrm{th}}^2} \right.
$$

$$
\left. - \frac{1 - e^{-2\pi F/v_{\mathrm{th}}^2}}{\int_0^{2\pi} \mathrm{d}x \, e^{\phi(x)/v_{\mathrm{th}}^2}} \int_0^{2\pi} \mathrm{d}x \left(e^{-\phi(x)/v_{\mathrm{th}}^2} \int_0^x \mathrm{d}x' \, e^{\phi(x')/v_{\mathrm{th}}^2} \right) \right]^{-1}, \tag{1.49}
$$

$$
= \frac{2\pi v_{\mathrm{th}}^2 (1 - e^{-2\pi F/v_{\mathrm{th}}^2})}{\int_0^{2\pi} \mathrm{d}x \, e^{\phi(x)/v_{\mathrm{th}}^2} \int_0^{2\pi} \mathrm{d}x \, e^{-\phi(x)/v_{\mathrm{th}}^2} - (1 - e^{-2\pi F/v_{\mathrm{th}}^2}) \int_0^{2\pi} \mathrm{d}x \left(e^{-\phi(x)/v_{\mathrm{th}}^2} \int_0^x \mathrm{d}x' \, e^{\phi(x')/v_{\mathrm{th}}^2} \right)}. \tag{1.50}
$$

Applying linear response theory[3, p. 289] by taking $F \to 0$, $\langle v \rangle = \lim_{F \to 0} F \mu$, μ is the mobility, and $e^{-2\pi F/v_{\mathrm{th}}^2} \to 1 - 2\pi F/v_{\mathrm{th}}^2$, gives us

$$
\gamma \mu = \lim_{F \to 0} \frac{\gamma \langle v \rangle}{F} \tag{1.51}
$$

$$
\Rightarrow \gamma \mu = \frac{2\pi \quad 2\pi}{\int_0^{2\pi} \mathrm{d}x \, e^{U(x)/v_{\mathrm{th}}^2} \int_0^{2\pi} \mathrm{d}x \, e^{-U(x)/v_{\mathrm{th}}^2}} \tag{1.52}
$$

We can now apply this result to a simple cosine potential, $mU(x) = \pm d\cos(x)$ (the sign does not matter and mass m will be set to one). The (co)sine is the most basic representation of wells and barriers in more realistic systems. Inserting $U(x) = d\cos(x)$ in equation (1.52) leads to

$$\gamma\mu = \frac{1}{I_0\left(d/v_{th}^2\right)^2},\tag{1.53}$$

where $I_0(x)$ is the modified Bessel function of the first kind. However, numerical integration allows us to use any tabulated periodic potential $mU(x)$. This makes equation (1.52) – in the limit of large frictions – quite powerful.

It is known[3, 4], that the more general theory of Green-Kubo relations predicts

$$D = \gamma\mu D_{free},\tag{1.54}$$

for any periodic potential, where the diffusion constant for the free Brownian motion is $D_{free} = k_B T/(m\gamma)$. For large friction constants γ, we have therefore derived an analytic equation for the diffusion constant D.

The following section considers a different limit – the limit of low temperatures.

1.3 Kramers' Rate Theory

Kramers' rate theory[5] considers one classical particle trapped in a potential hole and its escape due to random forces (Brownian motion). It was introduced to describe chemical reactions using transition state theory (TST).
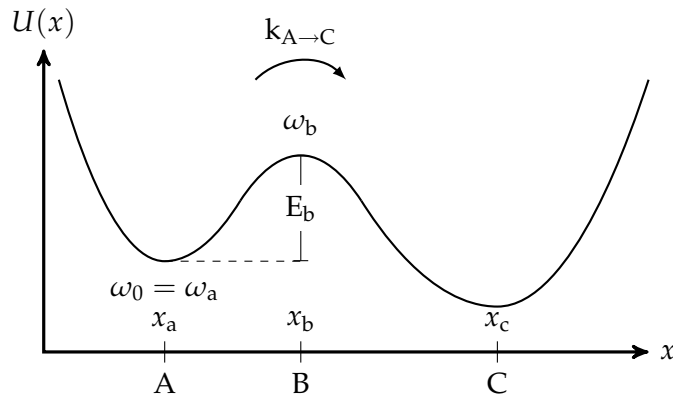

Figure 1.1: Potential $U(x)$ with two metastable states A and C. A particle inside the A-well can escape over the barrier at B. The barrier height is E_b. The escape occurs with the rate $k_{A\to C}$.

Kramers studies an asymmetric double well potential $U(x)$, schematically plotted in figure 1.1, and the Langevin equation (1.1). If the thermal energy $k_B T$ is much smaller than the barrier height E_b,

$$k_B T \ll E_b, \tag{1.55}$$

the random force acts only as a small perturbation and its influence can be neglected on the time scale of an unperturbed, damped motion, resulting in[2]

$$m\ddot{x} = -\frac{d}{dx} U(x) - \gamma m\dot{x}. \tag{1.56}$$

This system will relax to one of the minima and stay there for a long time $\propto e^{E_b/k_B T}$, before eventually the random force will drive the system over the barrier into a neighboring metastable state. The average of the escape time τ results in an escape rate

$$k_{A \to C} = \frac{1}{\tau}. \tag{1.57}$$

Following reference [5], we consider a stationary situation in which a steady probability current from A to C is maintained by sources and sinks. In particular:

- supply the A-well with particles (particle energy $\ll$ barrier height) and

- remove particles beyond the barrier.

The total probability flux j over the barrier is then given by the product of $k_{A \to C}$ and the population of the A-well, n_A

$$j = k_{A \to C} \cdot n_A \Leftrightarrow k_{A \to C} = \frac{j}{n_A}. \tag{1.58}$$

For the construction of a stationary current with probability density $\rho(x, v, t) \equiv \rho(x, v)$, we require that neither sources nor sinks should exist at the barrier. Further, we require $\rho(x, v)$ to obey the stationary Fokker-Planck equation around the barrier at B ($x \approx x_b$),

$$0 = \frac{\partial}{\partial t} \rho(x, v) = \left[-\frac{\partial}{\partial x} v + \frac{\partial}{\partial v} \left(\frac{1}{m} \frac{d}{dx} U(x) + \gamma v \right) + \gamma v_{th}^2 \frac{\partial^2}{\partial v^2} \right] \rho(x, v). \tag{1.59}$$

With x confined to a small neighborhood around the barrier top and

$$\omega_b^2 = -\frac{1}{m} \frac{d^2}{dx^2} U(x) \Big|_{x=x_b} > 0,$$

---

[2]In contrast to the previous sections, we do not include the mass m in the potential $U(x)$.

18

we approximate the potential to

$$U(x) \approx U(x_{\mathrm{b}}) - \frac{1}{2}m\omega_{\mathrm{b}}^2 (x - x_{\mathrm{b}})^2.$$ (1.60)

Equation (1.59) then reads

$$0 = \left[-\frac{\partial}{\partial x}v + \frac{\partial}{\partial v} \left(-\omega_{\mathrm{b}}^2 (x - x_{\mathrm{b}}) + \gamma v \right) + \gamma v_{\mathrm{th}}^2 \frac{\partial^2}{\partial v^2} \right] \rho(x, v).$$ (1.61)

We use Kramers' ansatz[5] for $\rho(x, v)$,

$$\rho(x, v) = \zeta(x, v) \exp\left[-\frac{\frac{1}{2}mv^2 + U(x)}{k_{\mathrm{B}}T} \right],$$ (1.62)

in equation (1.61) to obtain

$$0 = \left[-\frac{\partial}{\partial x}v + \frac{\partial}{\partial v} \left(-\omega_{\mathrm{b}}^2 (x - x_{\mathrm{b}}) + \gamma v \right) + \gamma v_{\mathrm{th}}^2 \frac{\partial^2}{\partial v^2} \right] \zeta(x, v) \exp\left[-\frac{\frac{1}{2}mv^2 + U(x)}{k_{\mathrm{B}}T} \right].$$ (1.63)

With

- $\frac{\partial}{\partial x}\left[v\zeta(x,v)e^{-\frac{\frac{1}{2}mv^2+U(x)}{k_{\mathrm{B}}T}} \right] = ve^{-\frac{\frac{1}{2}mv^2+U(x)}{k_{\mathrm{B}}T}}\left[\frac{\partial}{\partial x}\zeta(x,v) - \frac{\omega_{\mathrm{b}}^2(x-x_{\mathrm{b}})}{v_{\mathrm{th}}^2}\zeta(x,v) \right],$

- $\frac{\partial}{\partial v}\left[\zeta(x,v)e^{-\frac{\frac{1}{2}mv^2+U(x)}{k_{\mathrm{B}}T}} \right] = e^{-\frac{\frac{1}{2}mv^2+U(x)}{k_{\mathrm{B}}T}}\left[\frac{\partial}{\partial v}\zeta(x,v) - \frac{v}{v_{\mathrm{th}}^2}\zeta(x,v) \right],$

- $\frac{\partial}{\partial v}\left[v\zeta(x,v)e^{-\frac{\frac{1}{2}mv^2+U(x)}{k_{\mathrm{B}}T}} \right] = e^{-\frac{\frac{1}{2}mv^2+U(x)}{k_{\mathrm{B}}T}}\left[v\frac{\partial}{\partial v}\zeta(x,v) + \zeta(x,v)\left(1 - \frac{v^2}{v_{\mathrm{th}}^2} \right) \right],$

- $\frac{\partial^2}{\partial v^2}\left[\zeta(x,v)e^{-\frac{\frac{1}{2}mv^2+U(x)}{k_{\mathrm{B}}T}} \right] = e^{-\frac{\frac{1}{2}mv^2+U(x)}{k_{\mathrm{B}}T}}\left[\frac{1}{v_{\mathrm{th}}^2}\left(-2v\frac{\partial}{\partial v} + \frac{v^2}{v_{\mathrm{th}}^2} - 1 \right)\zeta(x,v) \right.$
$$\left. + \frac{\partial^2}{\partial v^2}\zeta(x,v) \right],$$

equation (1.63) becomes equivalent to

$$0 = \left[-v\frac{\partial}{\partial x} - \left(\omega_{\mathrm{b}}^2(x - x_{\mathrm{b}}) + \gamma v \right)\frac{\partial}{\partial v} + \gamma v_{\mathrm{th}}^2\frac{\partial^2}{\partial v^2} \right] \zeta(x, v).$$ (1.64)

One solution of equation (1.64) is $\zeta(x, v) \equiv \zeta = \mathrm{const}$. This corresponds to thermal equilibrium without a diffusive process. Equation (1.64) also allows[5] one solution where $\zeta(x, v)$ is a linear combination of x and v,

$$u = (x - x_{\mathrm{b}}) + av.$$ (1.65)

We rewrite equation (1.64) to

$$0 = \left[-\left((1 + \gamma a)v + \omega_b^2 a(x - x_b) \right) \frac{\partial}{\partial u} \zeta(u) + \gamma v_{th}^2 a^2 \frac{\partial^2}{\partial u^2} \zeta(u) \right]. \tag{1.66}$$

Equation (1.66) looks like an ordinary differential equation if the factor belonging to the first derivative is proportional to u,

$$-\lambda u = (1 + \gamma a)v + \omega_b^2 a(x - x_b). \tag{1.67}$$

(We keep in mind that we are still considering $x \approx x_b$.) Equation (1.66) then leads to

$$\lambda u \frac{\partial}{\partial u} \zeta(u) + b \frac{\partial^2}{\partial u^2} \zeta(u) = 0, \tag{1.68}$$

(with $b = \gamma v_{th}^2 a^2$) and has the solution

$$\zeta(u) = \frac{1}{N} \int_0^u d\tilde{u} \exp\left[-\frac{\tilde{u}^2}{2} \frac{\lambda}{b} \right], \tag{1.69}$$

where the normalization constant ist determined to $N = \sqrt{\frac{\pi b}{2\lambda}}$. λ and a immediately follow from equations (1.65) and (1.67)

$$\lambda_\pm = -\frac{\gamma}{2} \pm \sqrt{\omega_b^2 + \frac{\gamma^2}{4}}, \tag{1.70}$$

$$a_\pm = -\frac{\lambda_\pm}{\omega_b^2}, \tag{1.71}$$

where we choose the plus sign to allow the integral in equation (1.69) to converge. $\zeta(x, v)$ is then

$$\zeta(x, v) = \sqrt{\frac{2\omega_b^4}{\pi \gamma v_{th}^2 \lambda_+}} \int_0^{(x-x_b) - \lambda_+ v/\omega_b^2} du \exp\left(-\frac{1}{2} u^2 \frac{\omega_b^4}{\gamma v_{th}^2 \lambda_+} \right). \tag{1.72}$$

Analogous considerations also apply for the A-well, where $x \approx x_a$, and

$$U(x) \approx U(x_a) + \frac{1}{2} m \omega_0^2 (x - x_a)^2, \tag{1.73}$$

$$\omega_0^2 = \frac{1}{m} \frac{d^2}{dx^2} U(x) \Big|_{x=x_a} > 0. \tag{1.74}$$

However, as stated above, the source at A provides the well with thermalized particles,

$$\rho(x,v) \propto \exp\left[-\frac{\frac{1}{2}mv^2 + U(x)}{k_B T}\right], \quad x \approx x_a, \forall v, \tag{1.75}$$

implying – with equation (1.62) – that

$$\zeta(x,v) = 1 \qquad \text{for } x \approx x_a, \forall v. \tag{1.76}$$

We directly obtain

$$n_A = \int_{A-\text{well}} dx\, dv\, \rho(x,v) = \frac{2\pi v_{th}^2}{\omega_0} \exp\left[-\frac{U(x_a)}{k_B T}\right] \tag{1.77}$$

and[6]

$$j = \int_{-\infty}^{\infty} dv\, v\rho(x_b,v) = \frac{\lambda_+}{\omega_b} v_{th}^2 \exp\left[-\frac{U(x_b)}{k_B T}\right] \tag{1.78}$$

where we used equations (1.62) and (1.72). Kramers' rate now follows from equation (1.58)

$$k_{A\to C} = \frac{\omega_0}{\omega_b}\frac{1}{2\pi}\left(\sqrt{\frac{\gamma^2}{4} + \omega_b^2} - \frac{\gamma}{2}\right)\exp\left[-\frac{E_b}{k_B T}\right]. \tag{1.79}$$

We can now apply this result to, a simple cosine potential, $U(x) = -d\cos(x)$. From equations (1.60) and (1.73) we obtain

$$\omega_b^2 = \omega_0{}^2 = \frac{d}{m} \tag{1.80}$$

and note that $E_b = 2d$. The rate $k_{A\to C}$ tells us how often – per time unit τ – the particle crosses the barrier, i.e., moves from one minimum by 2π to the next. From Einstein's equation for the diffusion constant D in one dimension follows,

$$\langle(x(t) - x(0))^2\rangle = 2Dt, \qquad \text{for} \quad t \to \infty \tag{1.81}$$

$$\Leftrightarrow (2\pi)^2 = 2D\tau, \tag{1.82}$$

where the second line uses the system's length and time unit. We therefore obtain

$$\Leftrightarrow \frac{2 \times (2\pi)^2}{2\tau} = D. \tag{1.83}$$

The factor of 2 in the numerator arises from the fact, that we consider a symmetrical potential and crossing occurs in both directions, resulting in a twice as big rate. Following from equation (1.57) and equation (1.79),

$$D = (2\pi)^2 k_{A \to C},\tag{1.84}$$

$$\Rightarrow D = 2\pi \left(\sqrt{\frac{\gamma^2}{4} + \frac{d}{m}} - \frac{\gamma}{2} \right) \exp\left[-\frac{2d}{k_B T} \right].\tag{1.85}$$

We finally use equation (1.54) to obtain a results for $\mu\gamma$,

$$\mu\gamma = \frac{2\pi\gamma}{v_{th}^2} \left(\sqrt{\frac{\gamma^2}{4} + \frac{d}{m}} - \frac{\gamma}{2} \right) \exp\left[-\frac{2d}{k_B T} \right].\tag{1.86}$$

We have derived an analytic expression for the diffusion constant in the limit of $k_B T \ll E_b$. A comparison of equation (1.53) and equation (1.86) is shown together with numerical results in section 3.1.

We started with the general description of one particle in a one-dimensional potential influenced by stochastic forces. The derivation of equation (1.25) is an important step for further calculations. In the limiting cases of high frictions and low temperatures, respectively, we found an analytic solution for the diffusion constant D. We test these results in chapter 3.1.

2 Simulation Methods

2.1 Molecular Dynamics

Molecular dynamics (MD) simulation is a technique for computing the equilibrium and transport properties of a classical many-body system. It is based on an approximation of known physics. A simple algorithm, the Euler algorithm, as well as the slightly more advanced velocity Verlet algorithm that is used in this thesis, is given in appendix A. A complete introduction into MD is beyond the scope of this work. Instead, the author refers to the introductory literature by Frenkel and Smit [4].

2.2 Hyper-MD

Voter introduced a method for accelerating molecular dynamics simulations of infrequent events in his 1997 papers[7, 8]. This method, Voter calls it hyper-MD, is based on transition state theory. In TST, the transition rate between states equals the flux through a dividing surface separating these states. This flux is an equilibrium property of the system and does therefore not require actual dynamics to be performed. Voter used hyper-MD to accelerate dynamics by modifying the potential and reestablishing the connection to the original system, in particular, to the original time scale.

TST assumes that each crossing of the dividing surface corresponds to a true reactive event, in which the system passes from one state to another and then loses all memory of this transition before the next event occurs. The rate constant is then often an extremely good approximation to the true rate for strongly coupled systems. Hyper-MD does not use any advanced knowledge of neither the dividing surfaces nor the states through which the system may evolve. Instead, the potential energy surface (PES) is modified in such a way, that the correct relative probabilities for escape are conserved. The potential modifications are derived from local properties of the Hessian matrix only.

Adding to the Potential $V(x)$ a continous, non-negative bias *boost* potential $\Delta V^{\mathrm{b}}(x)$, designed so that $\Delta V^{\mathrm{b}}(x) = 0$ where $\delta_{\mathrm{A}}(x) \neq 0^1$, i.e., the potential is unaffected at the transition state region, leads to a single *boosted* time step

$$\Delta t_i^{\mathrm{b}} = \Delta t^{\mathrm{MD}} \exp \left[\beta \Delta V^{\mathrm{b}} \left(x(t_i) \right) \right] \tag{2.1}$$

---

[1] $\delta_{\mathrm{A}}(x)$ is the Dirac delta function positioned at the boundary to state A.

and results in a total *boosted* time

$$t^{\text{b}} = \sum_i^{n_{\text{tot}}} \Delta t^{\text{MD}} \exp\left[\beta \Delta V^{\text{b}}\left(x(t_i)\right)\right],\tag{2.2}$$

where n_{tot} is the total number of MD steps, t_i the time at the ith MD step and $\beta = 1/k_{\text{B}}T$ the inverse of the temperature times the Boltzmann constant. The total boost factor is then given by

$$\frac{t^{\text{b}}}{t^{\text{MD}}} = \frac{1}{n_{\text{tot}}} \sum_{i=1}^{n_{\text{tot}}} \exp\left[\beta \Delta V^{\text{b}}\left(x(t_i)\right)\right],\tag{2.3}$$

with $t^{\text{MD}} = n_{\text{tot}} \Delta t^{\text{MD}}$. The ideal bias potential is required to

- give a large boost factor,

- vanish at all dividing surfaces,

- cause a low computational overhead,

- avoid utilizing any prior knowledge of the dividing surfaces or the available escape paths and

- to show uncorrelated events only.

These requirements are anything but easily to fulfil. In particular, the calculation of the Hessian matrix leads to a computational overhead. Although this original approach was successfully applied to simulations, for instance the diffusion of adatoms (see figure 2.1), numerous variations with approximations have been developed[9, 10]. Most adaptions, however, focus on different strengths of hyper-MD while neglecting less relevant artifacts[11, 12, 13, 14].

The derivation (or rather modeling) of the bias potential is the key task of the hyper-MD method. If successful, the simulation time can be extended by a few orders of magnitude without using more computer time. A few examples of bias potentials are given in figure 2.2 to visualize the idea. Hyper-MD has been applied in various fields and aims at accerlating unfrequent events. A similar approach, metadynamics, was presented by Laio and Parrinello [16]. It is questionable, whether such methods in general – while beautiful in theory – can be applied to complex systems. For instance, both hyper-MD and Metadynamics make use of the potential and its modifications to accelerate dynamics. With an increasing number of degrees of freedom, this potential becomes very complicated and rough. It is then generally not possible to fulfil the requirements for these methods, for example, ΔV^{b} always greater zero. Without prior knowledge of relevant information, e.g. dividing surfaces, a definition for ΔV^{b} or similar properties in other methods, will not be possible. Also, the total
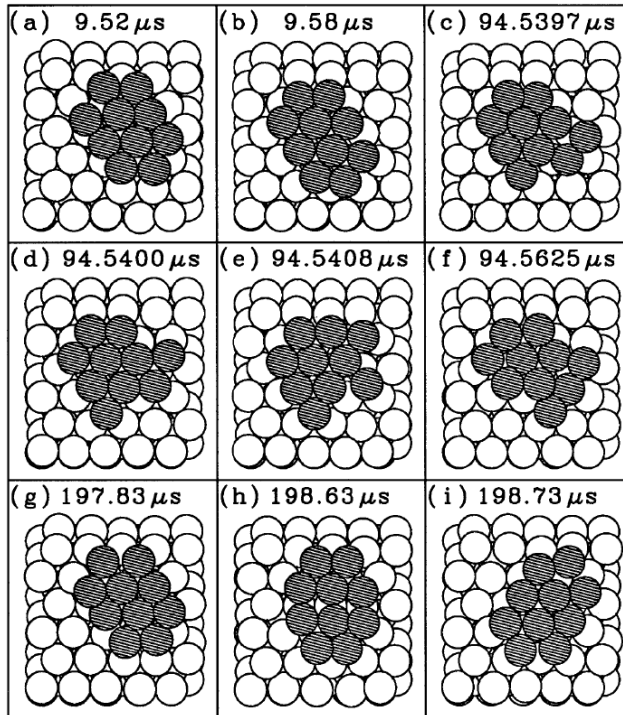
Figure 2.1: Simulation of a 10 atom Ag cluster on the Ag(111) surface. Boosted times t^b values – the boost ratio is over 8000[8] – are shown. The figure is taken from reference [8].

potential V in a many-body system is usually an implicit property. Its extraction is not trivial as shown in section 3.3.

In this work, we do not concentrate on the derivation of the bias potential ΔV^b, but rather use an existing potential to test the method in general. We take a one-dimensional potential as $V(x)$ and a modified potential as $V(x) + \Delta V^b(x)$.[2] Then, we compute a boosted time step Δt^b for each MD time step Δt^{MD} using equation (2.1), resulting in a total boosted time t^b. At the end of the simulation we compare both dynamics by analyzing the diffusion constants. Since the speed-up of t^{MD} (leading to t^b) is taken into account, we expect the diffusion constants of both runs to be the same. If they are not the same, the calculated speed-up – which would neutralize faster dynamics when obtaining the diffusion constant – must be wrong.
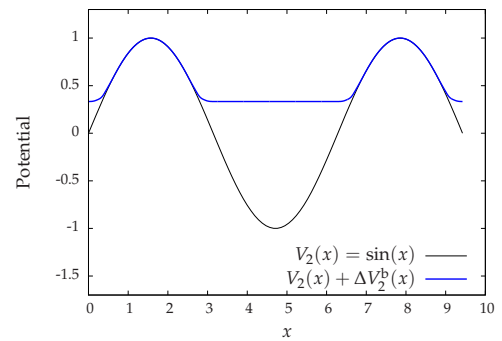
In section 3.2 the method is applied to two cases. The first one, where the potential in figure 2.2(b) is used as suggested in reference [11], should validate the method,

---

[2]The modification is done in such a way, that the manipulated potential offers lower barrier heights. Thus, we expect faster dynamics.
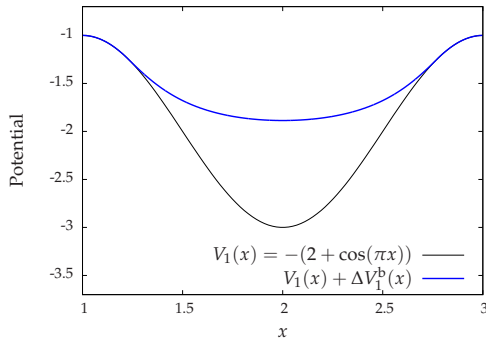
(a) A simple cosine and a boosted potential based on Rudd and Voter [15].

(b) A flat boosted potential by Steiner et al. [11].
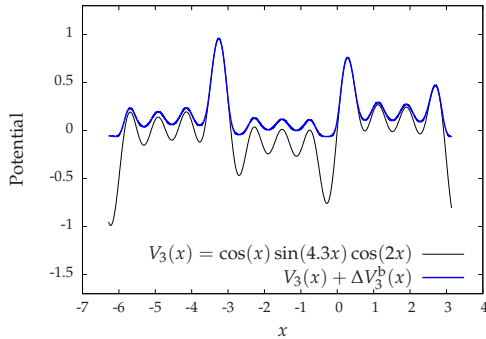
(c) An extension of Steiner's flat implementation by Hamelberg et al. [14]. The underlying shape of the potential is preserved.
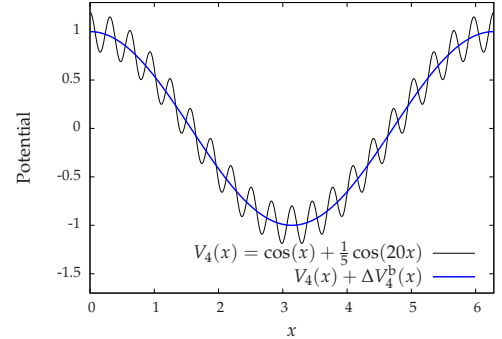
(d) A modulated cosine and the boosted plain cosine potential.

Figure 2.2: Different realizations of a boosted potential. (b) and (c) introduce errors due to disregarding TST requirements. However, (b) also offers obvious advantages: zero forces in the flat region reduce the computational effort. A completely different interpretation of a boosted potential is shown in (d).

while the second one, using the potential in figure 2.2(d), is closer to a situation one usually considers. As shown in the figure, the boosted potential is the "smoothened" form of the original potential. Smoothening, or averaging, the potential is the key property of a method called "coarse-graining". It is introduced in the following section.

2.3 Coarse Graining

A variety of quantum mechanical methods are used to address properties on a high-resolution microscopic level. However, they are limited to short length and time scales. Material properties of soft matter systems offer a big range of applications due to the variance of physical properties. The interplay of local chemical and global conformational properties makes soft matter macromolecues very flexible[17]. This means, that many different length and time scales are relevant. Coarse-graining is one method to overcome limits of simulations at a fixed scale. It stands for replacing a detailed description with a lower-resolution model by reducing the amount of degrees of freedom through averaging or smoothing out.

The link between different scales in multiscale simulations is given by parameters characterizing each level. These parameters are typically related to experiments. However, linking different scales is in general not obvious. Many different approaches have been followed, ranging from the quantum mechanical, via the classical, to the coarse-grained level[18].

Coarse-graining methods can be described by the physical quantities, which are supposed to be reproduced by the model on different levels. One distinguishes structure-, force- and potential energy based approaches. All approaches use the underlying model (e.g., all-atom) to determine the CG interactions. These interactions are derived by[18]

- (iterative) Boltzmann inversion of distribution functions,

- inverse Monte Carlo sampling or

- force matching.

The (different) resulting CG potentials therefore reproduce some physical quantities better than other. A recent study[19] compares these approaches and current research deals with the question, whether it is possible to derive CG potentials that are both thermodynamically as well as structurally consistent with the underlying model[18]. Nevertheless, coarse-graining is not only used to obtain structural information. Its goal is also to allow a better understanding of the dynamics of the considered system.

The next section introduces the coarse-grained model for polystyrene. In chapter 3.4, simulations of polystyrene based on both the atomistic, which is taken from reference [20], as well as the coarse-grained model follow.

2.3.1 Coarse-Grained Model of Polystyrene

The model in reference [2] was used for all coarse-grained simulations of polystyrene (chemical formula: C_8H_8) in chapter 3. A quick summary follows.

For the derivation of the model, Fritz et al. assume, that the total potential energy U^{CG} for a CG chain can be split in a bonded and nonbonded part

$$U^{\mathrm{CG}} = \sum U^{\mathrm{CG}}_{\mathrm{bond}} + \sum U^{\mathrm{CG}}_{\mathrm{nonbonded}}. \tag{2.4}$$

The methodology is described and summarized in four steps.

1. Atomistic simulations of isolated random walks are performed. Only local interactions are taken into account.

2. The distribution functions $P^{\mathrm{CG}}(r, \theta, \phi, T)$ are calculated. These are functions of the CG bond length r, bending angles θ and dihedral angles ϕ.

3. Using inverse Boltzmann relations, the CG bonded potentials read

$$U^{\mathrm{CG}}(r, T) = -k_{\mathrm{B}}T \ln \left(P^{\mathrm{CG}}(r, T)/r^2 \right), \tag{2.5}$$

$$U^{\mathrm{CG}}(\theta, T) = -k_{\mathrm{B}}T \ln \left(P^{\mathrm{CG}}(\theta, T)/\sin(\theta) \right), \tag{2.6}$$

$$U^{\mathrm{CG}}(\phi, T) = -k_{\mathrm{B}}T \ln \left(P^{\mathrm{CG}}(\phi, T) \right). \tag{2.7}$$

4. Effective nonbonded potentials in a tabulated form are added to complete the CG force field.

The used mapping scheme was originally introduced by Harmandaris et al. [21]. Each monomer is mapped onto two coarse-grained, spherical beads of different types. Quoting reference [2]:

> **Bead A** contains carbon atoms in the backbone connecting two subsequent phenyl rings and hydrogen atoms attached to these carbon atoms. The CH groups in the backbone to which the phenyl rings are attached, belong to two neighboring beads. The center of bead A is the center of mass of the CH_2 group and the two CH groups, which are taken into account with half of their masses.

> **Bead B** contains the atoms of the phenyl group. The center of bead B is mapped onto the center of mass. The beads are connected by CG bonds A-B between the alternatig types of beads. This leads to a chain without side groups. There are no bonds A-A or B-B between neighboring beads of the same type.

The mapping scheme is shown in figure 2.3(a). In order to study the angular diffusion of polystyrene, we limit our polymer in its spatial dimension.
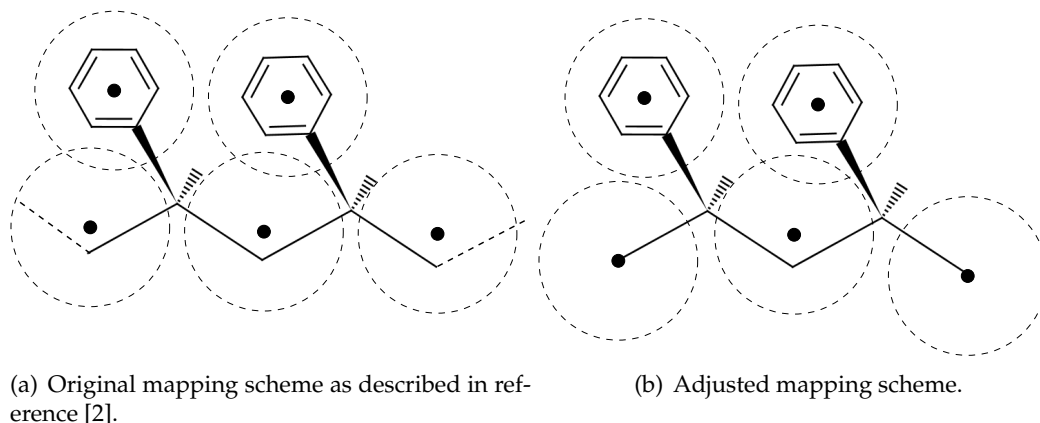
(a) Original mapping scheme as described in reference [2].

(b) Adjusted mapping scheme.

Figure 2.3: Visualization of the performed adjustments. (a) shows the original mapping scheme. It is continued to both directions. This thesis' scheme only consisting of two phenyl rings is shown in (b).

This thesis uses an adjusted mapping scheme with only two phenyl rings and their connecting CH_2 group. Instead of continuing the polymer to both directions by attaching another CH_2 group, we replace these by CH_3 groups and saturate all valencies. Secondly, the mapping points at the ends of our oligomer coincide with the C atoms. The adjusted scheme is shown in figure 2.3(b). The coarse-graining process is visualized in figure 2.4. This adjustment is purely geometric (implying different in-

(a) Atomistic

(b) Towards CG

(c) Coarse-grained
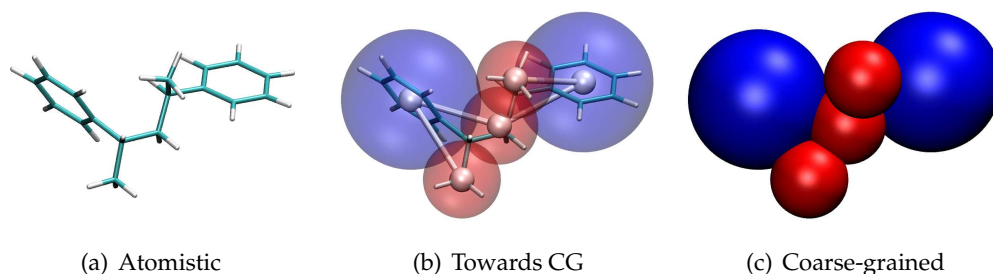
Figure 2.4: A polystyrene dimer in different representations. The all-atom model is shown in (a). Atoms and parts of atoms are grouped into beads, visualized in (b). The resulting CG description (c) contains only A (red spheres) and B (blue spheres) beads. The white beads and bonds in (b) indicate the "new" backbone.

teractions due to modified distances). Its effects and possibly introduced errors have not been studied. A future analysis should cover a systematic investigation of differences between large polymers and short oligomers as well as different orientations. We limit our effort to an isotactic – both phenyl rings are pointing to the same side –

chain. The reason for these adjustments is to keep the system as simple as possible. Nevertheless, it provides information about the angular diffusion. Results follow in the next chapter.

3 Results

3.1 One Dimensional Diffusion

Computer stochastic dynamics simulations have been performed to confirm the analytic results of chapter 1. The simulations are based on the algorithm presented in appendix A. The results in this section have been confirmed by using the *ESPResSo*[22] package.

All values are presented in reduced Lennard-Jones units (see table 3.1). To simplify tests, the particle's mass m was set to one. Each simulation data point was obtained by fitting the mean square displacement (MSD) for x according to equation (1.81) using *Mathematica*[23].

Quantity	Symbol	Relation to SI
Length	r^*	$r\,\sigma^{-1}$
Mass	m^*	$m\,M^{-1}$
Energy	E^*	$E\,\epsilon^{-1}$
Temperature	T^*	$k_B T\,\epsilon^{-1}$
Time	t^*	$t\,\sigma^{-1}\sqrt{\epsilon/M}$

Table 3.1: Reduced Lennard-Jones units. M is the total mass of the system (here: always set to one). ϵ defines the energy scale, σ the length scale.

Figure 3.1 shows the results obtained from the Smoluchowski limit (equation (1.53)), Kramer's rate theory (equation (1.86)) and the simulation data for different friction constants γ. The figure shows how the Smoluchowski limit is slowly approached for increasing friction constants reaching a very good agreement for $\gamma = 5.0$. Kramers' result is also plotted over the full range of temperature. As expected, this theory leads to good agreement for small temperatures only. The limit of its validity depends on γ. Figure 3.2 shows the data for small temperatures and allows us to take a closer look at the results from Kramers' theory. For $\gamma = 0.1$, Kramers underestimates the diffusion at temperatures higher than 0.3. With higher friction, the agreement improves and reaches its maximum for $\gamma = 0.5$. Further increasing the friction constant leads to an overestimation at temperatures above 0.3. For better comparison, this data is also numerically shown in appendix D. The numerical results for the cosine potential agree with Risken [3], p. 319.

Furthermore, numerical integration allows us to apply equation (1.52) to any periodic potential. A modulated cosine potential, $U(x) = \cos(x) + \frac{1}{5}\cos(20x)$, was chosen as another example. The results are shown in figure 3.3. For this potential, good agreement is reached more slowly. For $\gamma = 5.0$, the deviation between simulation data and calculation is notably larger than for the plain cosine.

Although this approach is promising at first sight, its disadvantage is rather obvious: it is limited to large friction constants. However, it is useful for testing conceptual ideas.

An application of Kramers' rate theory for the modulated cosine is not directly possible. $U(x)$ would lead to two escape rates – one for the first and one for the second, high-frequency cosine term. Combining these two rates was not covered in this thesis. It is already clear at this point, that Kramers' rate theory can not be efficiently applied to more complex periodic potentials: every barrier would need special attention.
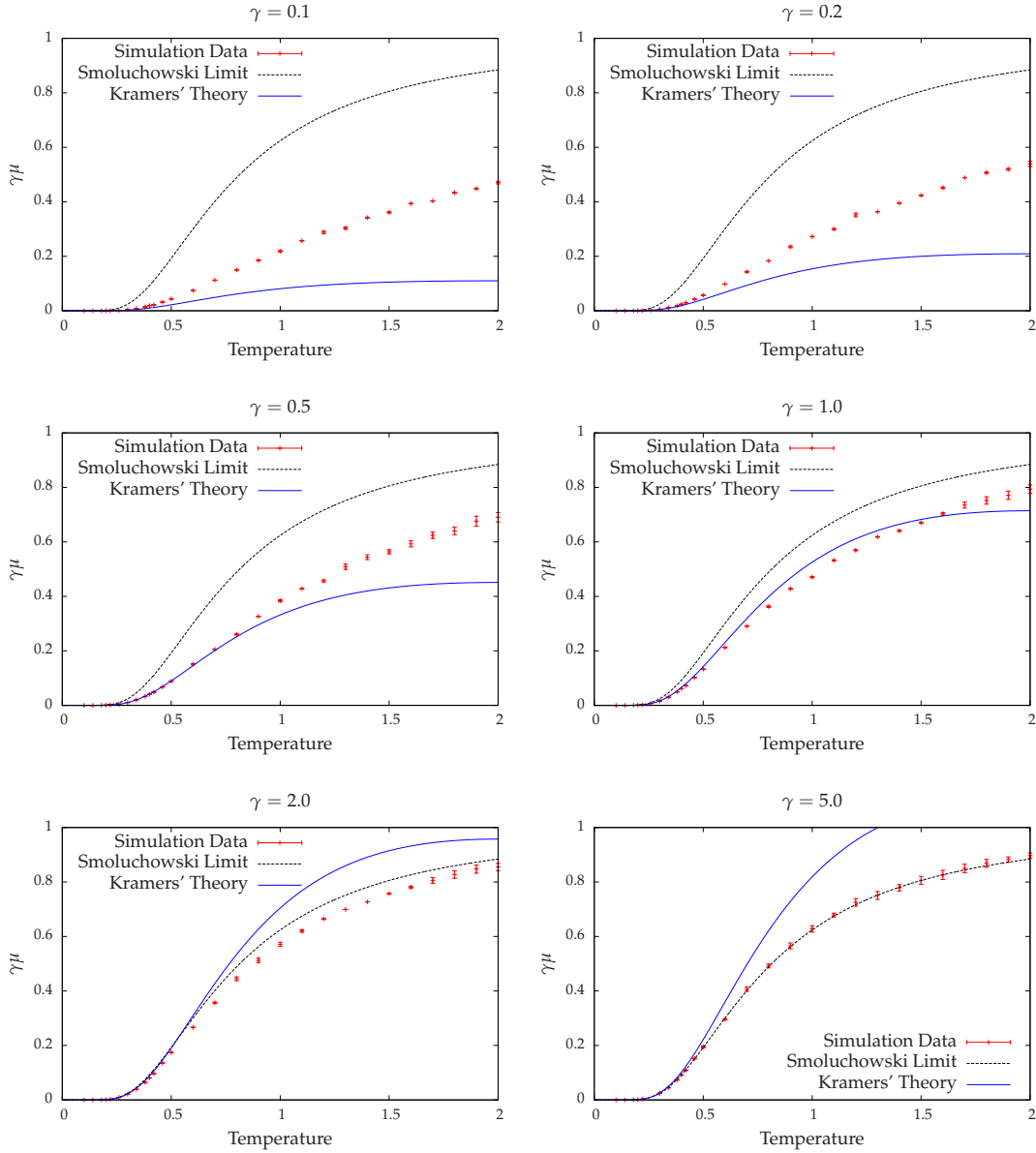
Figure 3.1: Simulation data and analytic results for the potential $U(x) = -\cos(x)$. The mobility times the friction is shown as a function of the temperature for different friction constants. Each plot shows 28 single simulations.

Figure 3.2: Simulation data and analytic results for the potential $U(x) = -\cos(x)$ and small temperatures. The mobility times the friction is shown as a function of the temperature for different friction constants. Each plot shows 13 single simulations.

Figure 3.3: Simulation data and analytic results for the potential $U(x) = \cos(x) + \frac{1}{5}\cos(20x)$. The mobility times the friction is shown as a function of the temperature for different friction constants. Each plot shows 28 single simulations.
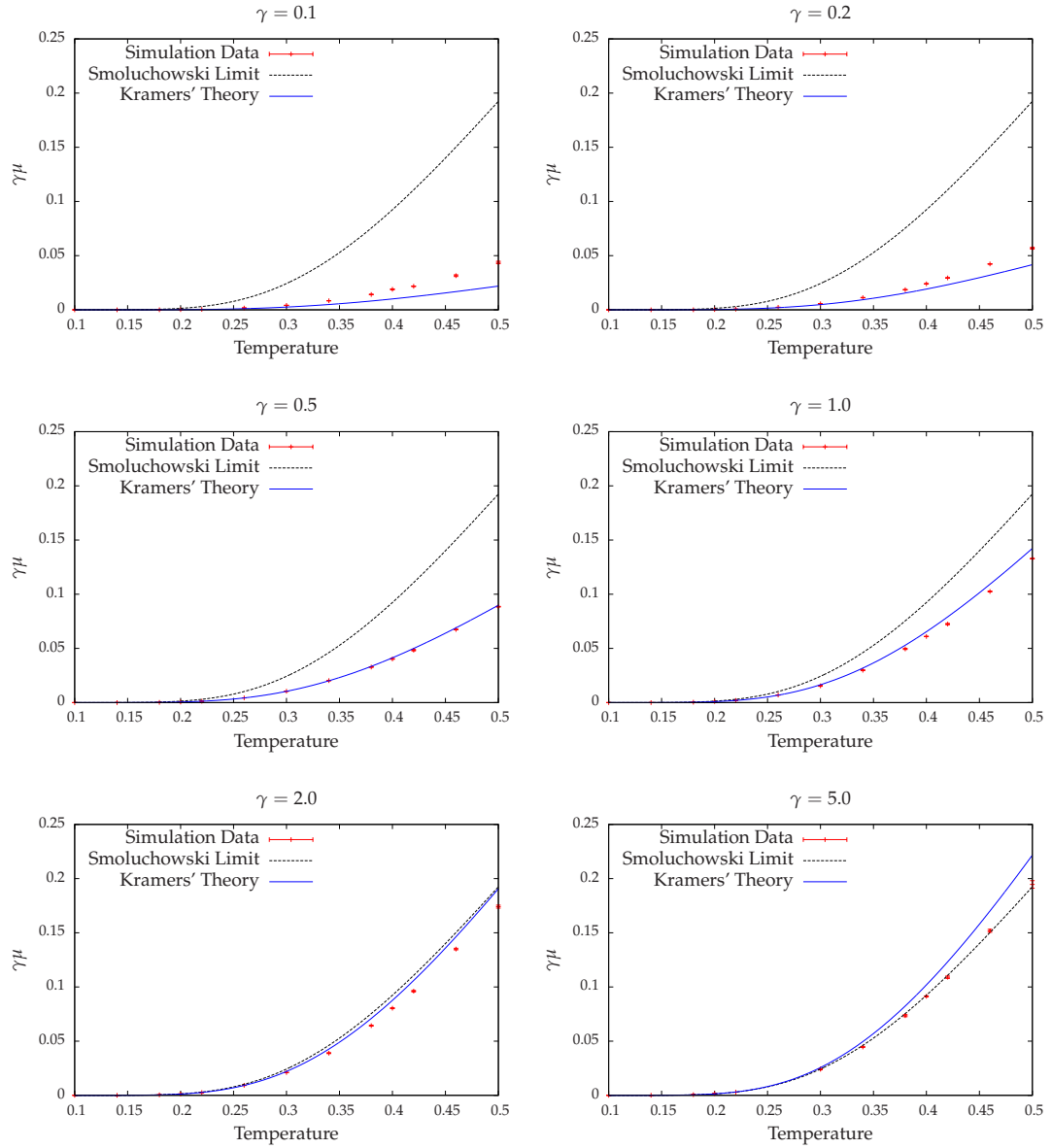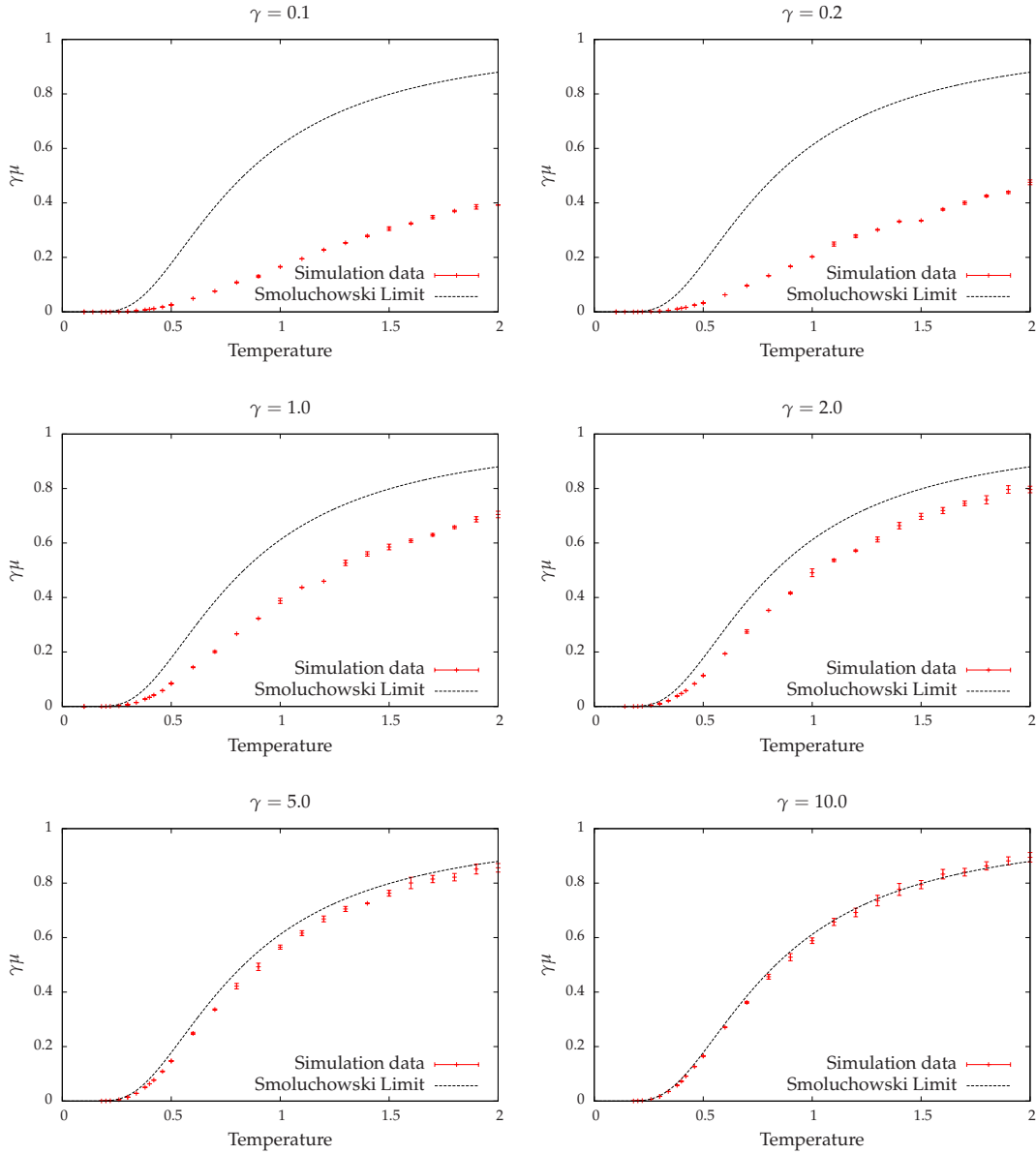
3.2 Boosted Dynamics Using Hyper-MD

Based on the theory of section 2.2, the previously used simulation program was modified in order to take the "boost" between two potentials into account. It was applied to the potentials in figure 2.2(b) (plain cosine and Steiner's implementation of a boosted potential) and 2.2(d) (modulated cosine and a plain cosine as the smoothened, boosted potential), respectively. First, we study the case for $\gamma = 1.0$ and temperatures T=0.5 and T=1.0, respectively.

The results for the plain cosine are shown in figure 3.4 and table 3.2. This potential was used to validate the method. The data denoted as "MD" corresponds to a regular MD simulation including stochastic forces, while "Hyper-MD" was obtained using the boosted potential and taking the boosted time into account. In principle, both should lead to the same diffusion constant. This is because we compensate the speed-up of the dynamics by accelerating the time (i.e., increase the time step) according to equation (2.1). The advantage of hyper-MD is then the extended time scale. In particular, figure 3.4(a) shows the mean square displacement as a function of time for the temperature of 0.5. The same amount of simulation steps leads – using h-MD – to a roughly five times longer time scale. Figure 3.4(b) confirms the approximate equality of the diffusion. However, for the temperature of 1.0, figures 3.4(c) and (d) show significant deviations. Firstly, the time scale is extended by a factor of roughly two, reducing the benefit of hyper-MD drastically. Secondly, h-MD fails to compensate the boost factor correctly and underestimates the dynamics. The bias potential ΔV violates the requirements for transition state theory and might thereby cause the shown deviations[11].

Temperautre	Method	D	Time Scale
0.5	MD	0.0616(1)	2.0×10^4
	H-MD	0.0562(1)	1.1×10^5
1.0	MD	0.4796(7)	2.0×10^4
	H-MD	0.4258(4)	4.0×10^4

Table 3.2: Numerical results of figure 3.4 – hyper-MD based on Steiner. The friction constant γ and the mass m were set to one.

Figure 3.5 and table 3.3 show the results for the modulated cosine. The modulated cosine mimics a rough potential surface. The underlying (unmodulated) cosine represents the corresponding smoothened potential surface – similar to coarse-graining. In other words, we test hyper-MD for the key property of the coarse-graining method. While the diffusion constants in figures 3.5(b) and (d) show a similar behavior to the
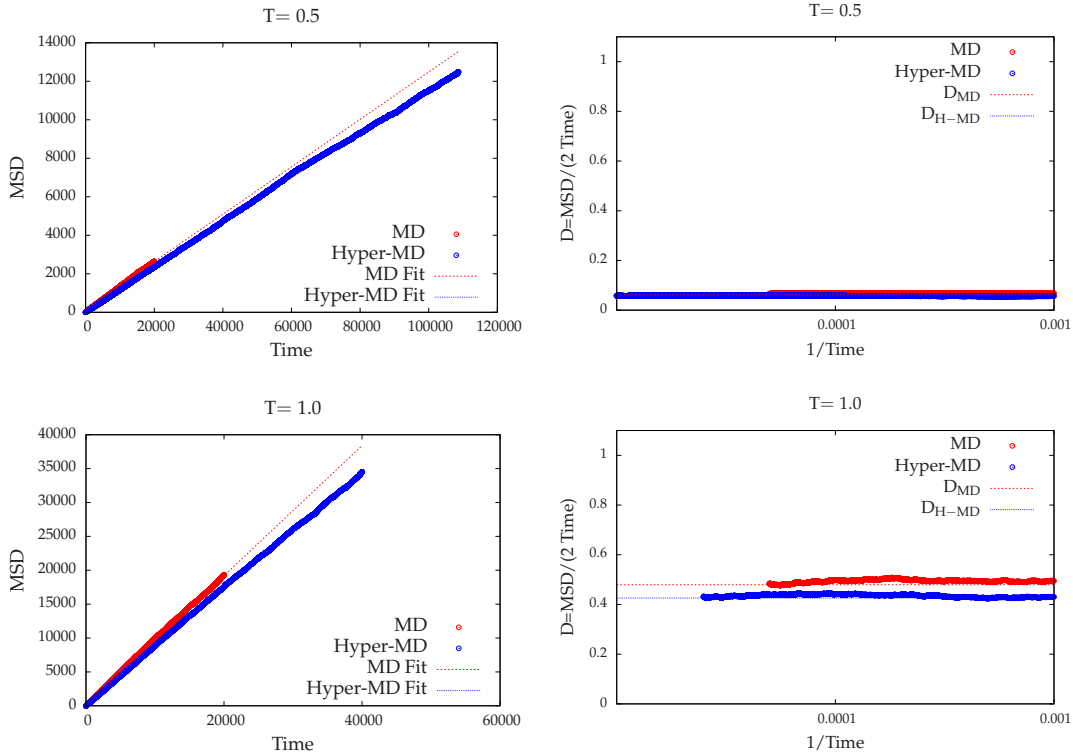
Figure 3.4: Hyper-MD results for a plain cosine and Steiner's boosted potential for different temperatures. The potential is shown in figure 2.2(b). The plots on the left side show the mean square displacement as a function of the time together with the least-squares fit. The plots on the right side show the corresponding diffusion constants. The friction constant γ was set to one.

previous potential[1], the MSD plots indicate an important difference: the time scale is not extended. This is due to the fact that we neglect a requirement, namely ΔV^b always greater zero. As a consequence of the symmetry of the considered potential, equation (2.1) leads to a likewise speed-up (positive ΔV^b) and slow-down (negative ΔV^b) of t^b. The single contributions sum up to a speed-up of roughly zero.

These simulations were repeated for both potentials over a wide range of friction constants and temperatures. Their results are shown in figures 3.6 and 3.7. The difference in diffusion constants of both methods increases with higher temperatures and friction constants. In the case of Steiner's implementation for the boosted potential, h-MD underestimates the diffusion constant (by overestimating the time boost). In contrast, h-MD overestimates the diffusion for the modulated cosine potential

---

[1]H-MD overestimates the diffusion constant this time.

Temperautre	Method	D	Time Scale
0.5	MD	0.0359(1)	2.0×10^4
	H-MD	0.0602(1)	2.0×10^4
1.0	MD	0.3785(6)	2.0×10^4
	H-MD	0.4812(7)	2.0×10^4

Table 3.3: Numerical results of figure 3.5 – hyper-MD for the modulated cosine. The friction constant γ and the mass m were set to one.

$U(x) = \cos(x) + \frac{1}{5}\cos(20x)$. However, for the latter, the difference in diffusion constants does not depend on the temperature. These distinct behaviors were not further examined. A future study should investigate the influence of violated requirements for the bias potential.

We recap above observations: Hyper-MD is not always able to correctly include the speed-up of dynamics in the speed-up of the time. The boosted potentials used in this section violate the requirements and consequently lead to deviations in their results. However, we still used simple model potentials – models describing a given chemical system more precisely are yet more unlikely to fulfil the assumptions of h-MD. Furthermore, the characteristic property of CG is a smoothened potential surface of the original description. Smoothening also lowers barrier heights and therefore violates stated requirements. Strictly speaking, hyper-MD can not be applied to more realistic systems.

The presented methods use the previously obtained potential of the system. However, the potential of a many-body system is usually not explicitly given. Its extraction can be rather difficult, as the next section shows.
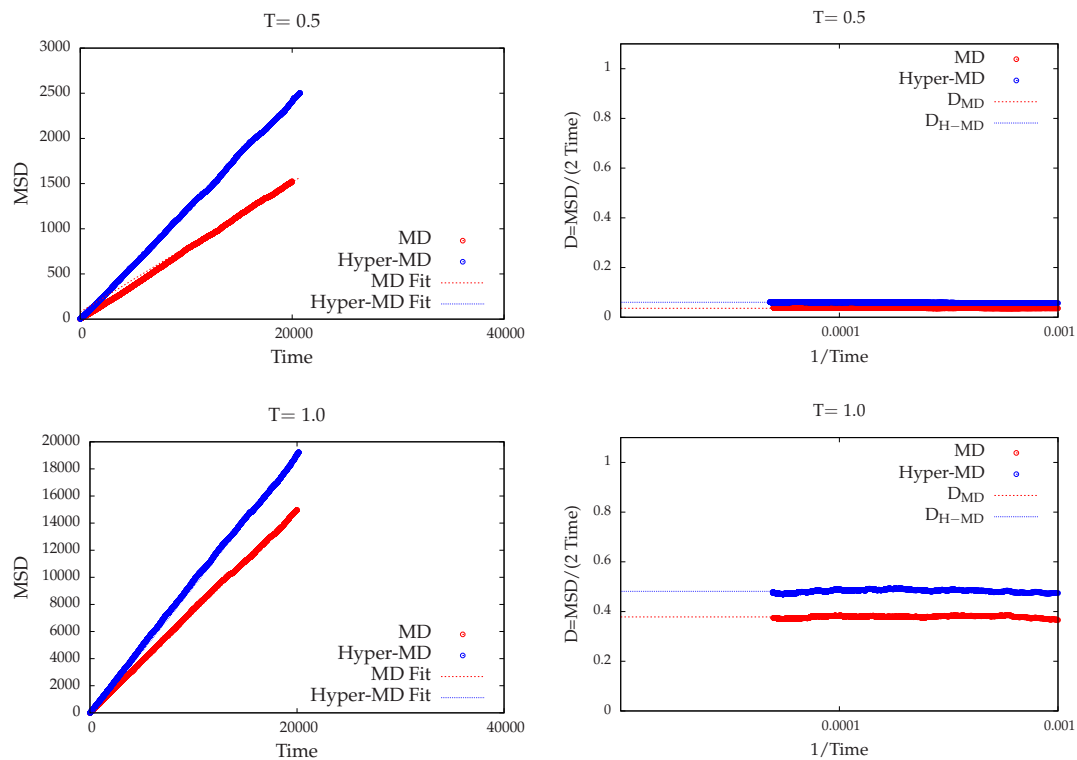
Figure 3.5: Hyper-MD results for a modulated cosine and a plain cosine as the boosted potential for different temperatures. The potential is shown in figure 2.2(d). The plots on the left side show the mean square displacement as a function of the time together with the least-squares fit. The plots on the right side show the corresponding diffusion constants. The friction constant γ was set to one.
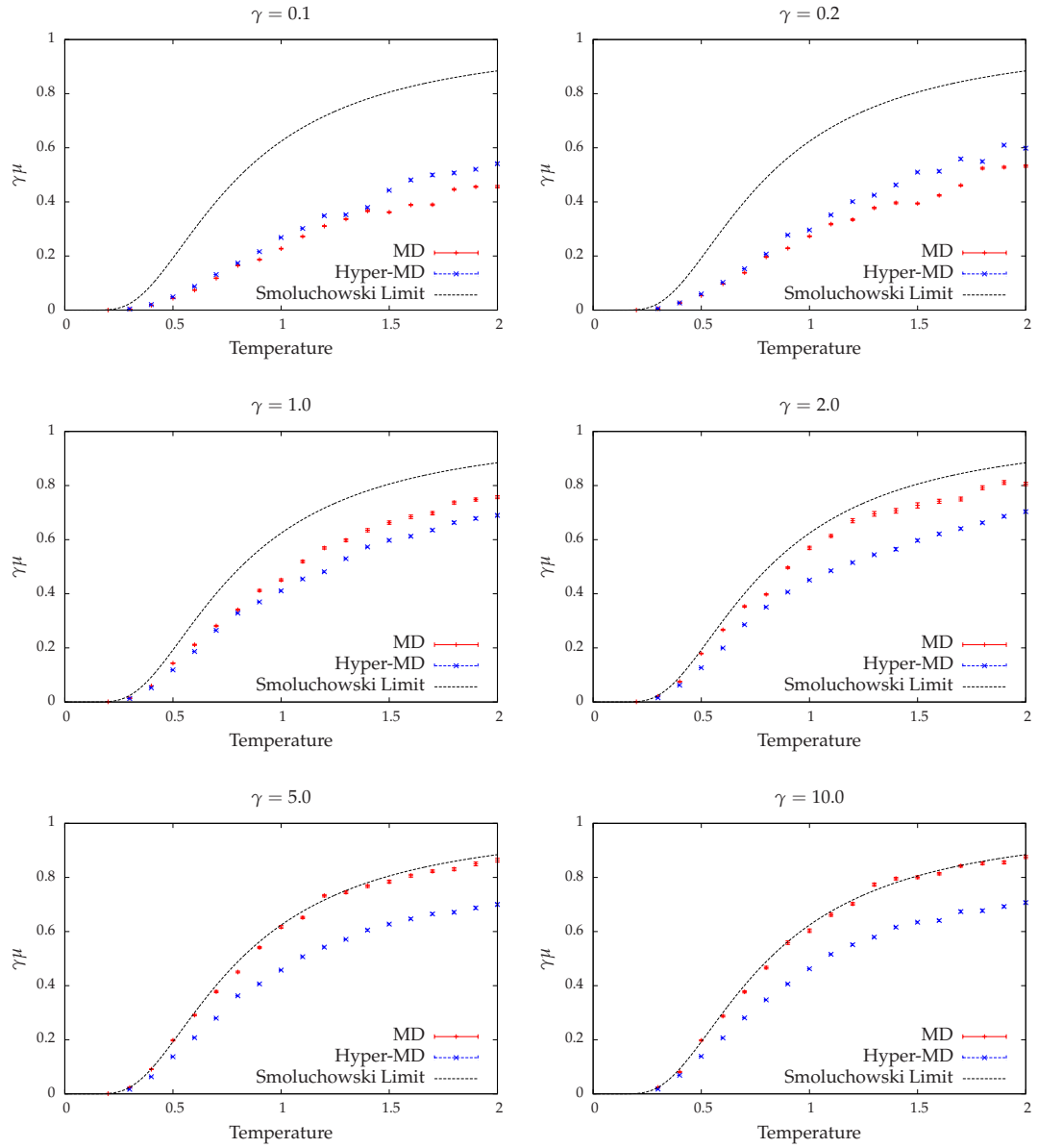
Figure 3.6: Regular MD and h-MD simulations for Steiner's boosted potential in figure 2.2(b). The particle's mass was set to one.
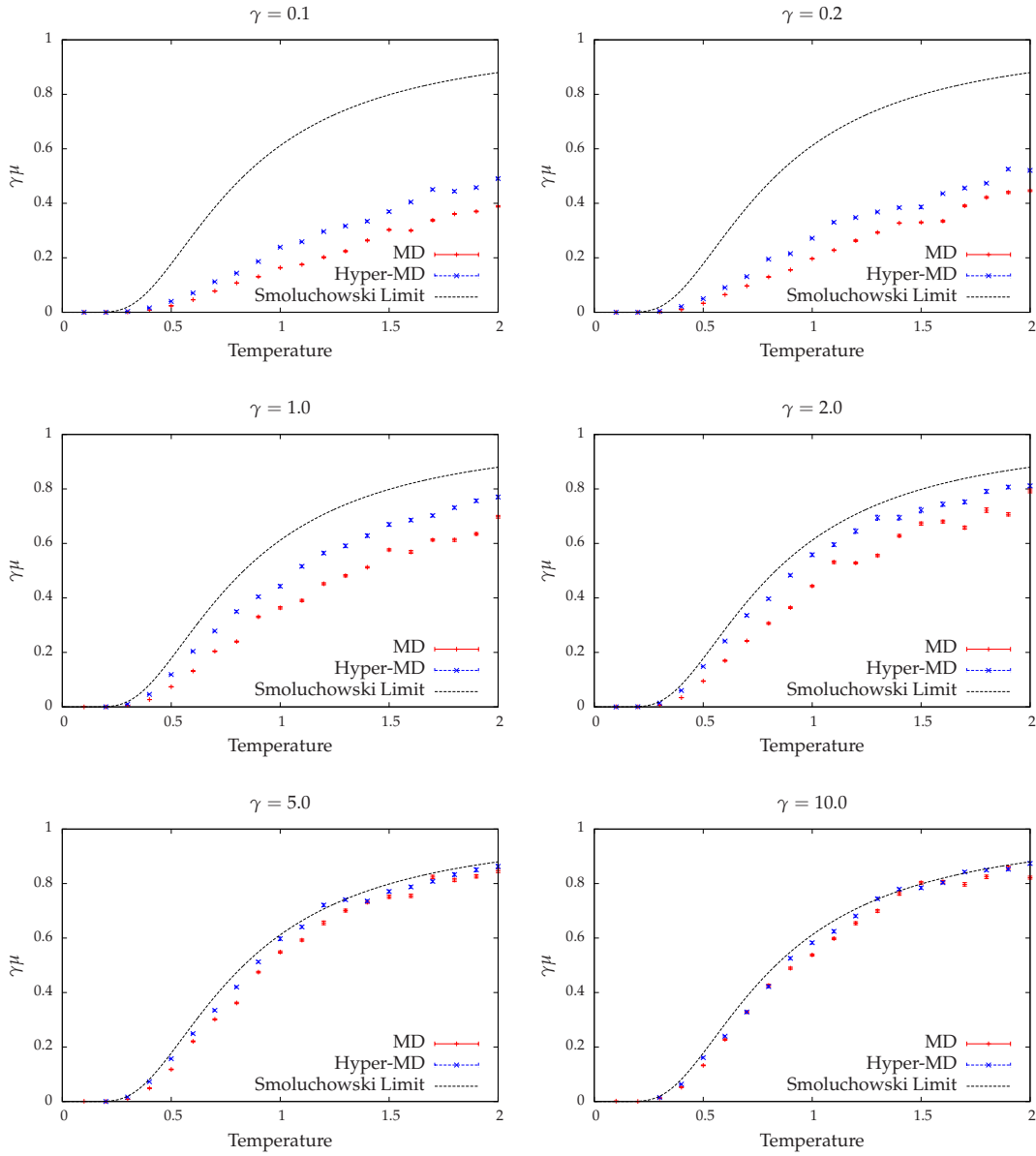
Figure 3.7: Regular MD and h-MD simulations for the modulated cosine potential in figure 2.2(d). The particle's mass was set to one.

3.3 Dihedral Potential Energy Surface

We would like to apply the introduced methods to the more realistic system of polystyrene. We study the dihedral potential of ψ_1 and ψ_2 (see figure 3.10) in both descriptions (see figure 2.4). *Gromacs*[24] is used for all simulations in this section.

(a) Atomistic PES

(b) Coarse-Grained PES
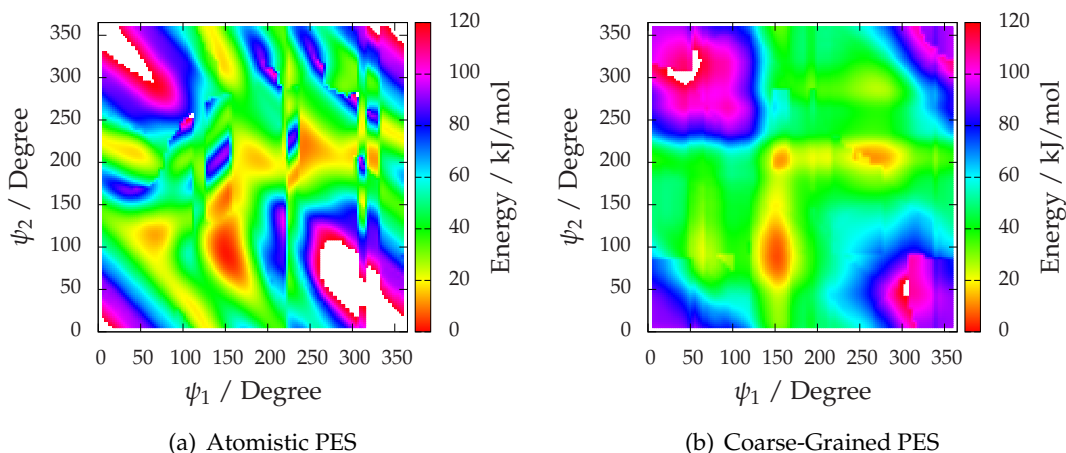
Figure 3.8: The potential energy surface for the atomistic and the coarse-grained description. Obtained using a MD simulation at T=0K (almost equivalent to steepest descent). Energy values in units of kJ/mol. Regions with energies above 120 kJ/mol appear white.

The dihedral potential energy surface of the CG model, shown in figure 3.8(b), confirms the results in reference [2]. It shows the expected symmetrical shape for the mirror plane going through ($\psi_1 = 0°$, $\psi_2 = 360°$) - ($\psi_1 = 360°$, $\psi_2 = 0°$). The energetically unfavorable regions at the "corners" of the plot correspond to the unfavorable conformation, where the molecule is confined to a plane. The minima are well defined and located at (150°, 85°), (150°, 200°), (280°, 200°) and surrounding angles.

The situation for the dihedral PES in the atomistic description, shown in figure 3.8(a), however, is certainly more complex. Firstly, we note the artifacts for $\psi_1 > 200°$. These dislocations along the ψ_2-axis are caused by the extraction method. For the extraction, ψ_1 was fixed at a certain degree and ψ_2 was rotated in steps of 5° with a subsequent energy minimization. However, due to the rough surface, the energy minimization (a simple MD simulation, i.e., no stochastic terms) did not always lead to the *energetically most favorable* configuration belonging to a local minimum. Instead, the system's all remaining degrees of freedom relaxed to the *closest* local minimum. From there, further rotating ψ_2 might lead to a very unfavorable configuration and forces the system to "flip". This explains why the dislocations occur along the ψ_2-axis.

Nevertheless, we neglect this dependance on the initial configuration and the resulting artifical deviations for a moment. From figure 3.8(a), we can still guess the symmetry together with the minima. We note the in general more detailed resolution of the potential and the maximum at $(25°, 175°)$, which does not appear in the CG dihedral PES. Particularly noticeable is the maximum at $(150°, 200°)$, which corresponds to a minimum in the CG plot. This leads to the conclusion, that coarse-graining not only smoothens the surface, but – due to the new geometry including the new effective potential – also changes the system fundamentally.

A more detailed description of the extraction method as well as further (unsuccessful) effort to get rid of the artifacts are shown in appendix B.

3.4 Angular Diffusion of Polystyrene

Figure 3.9 shows the mean square displacement $(\Delta\psi)^2$ for the atomistic as well as for the coarse-grained system (see equation (3.2) and figure 3.10 for the definition of $\Delta\psi$). The simulation runtime for the atomistic model was doubled, since the dynamics was expected to be slower than the dynamics in the coarse-grained model. The data for both models were obtained in a stochastic dynamics simulation at T=503K using *Gromacs*[24] . The friction constant γ was set according to $\gamma = \frac{1}{0.01\ \text{ps}}$. A complete listing of the input parameters are shown in section C.
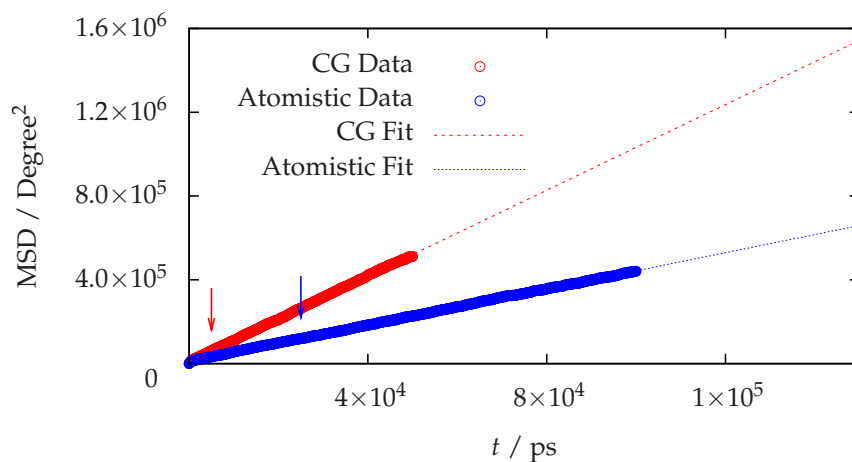
Figure 3.9: Regular mean square displacement plot. The single data dots appear as a solid line due to their enormous number. The dashed lines indicate the linear fitting model from equation (3.4), the arrows mark the starting points for the fitting routine.

Einstein's relation in one dimension,

$$\lim_{t \to \infty} \left\langle (\Delta x)^2 \right\rangle = 2 D_x t, \tag{3.1}$$

where $\Delta x = x(t) - x(0)$, the brackets $\langle \rangle$ denote an ensemble average and D_x is the diffusion coefficient for the x-coordinate, is used for both dihedrals ψ_1 and ψ_2 (see figure 3.10), with
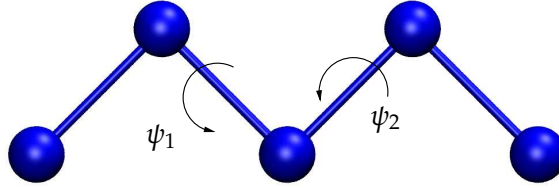
Figure 3.10: The dihedral angles in the CG model of polystyrene. They are mapped to the atomistic description according to figure 2.4(b).

$$(\Delta \psi)^2 = (\Delta \psi_1)^2 + (\Delta \psi_2)^2, \tag{3.2}$$

and extended to two dimensions. This results in

$$\lim_{t \to \infty} D_\psi = \frac{1}{2 \cdot 2t} \left((\Delta \psi_1)^2 + (\Delta \psi_2)^2 \right) \tag{3.3}$$

and suggests

$$(\Delta \psi_1)^2 + (\Delta \psi_2)^2 = 4 D_\psi t \tag{3.4}$$

to fit our data for large t. The fit results using equation (3.4)[2] are also shown in figure 3.9 and the following diffusion coefficients were obtained[3] (in units of squared degrees per picosecond):

$$D_\psi^{\text{cg}} = 2.5560(2)$$
$$D_\psi^{\text{at}} = 1.0804(1) \quad \text{and}$$
$$\zeta \equiv D_\psi^{\text{cg}} / D_\psi^{\text{at}} = 2.3657(3). \tag{3.5}$$

A higher angular diffusion coefficient implies faster dynamics for that particular degree of freedom. As expected, coarse-graining polystyrene speeds up the angular diffusion (among others).

---

[2]Equation (3.4) was modified to $4 D_\psi t + y_0$.
[3]Simple propagation of uncertainty was used in equation (3.5).

In a log-log plot, the difference in diffusion coefficients becomes an additive number,

$$\log \mathrm{MSD}_\psi = \log 4 \underbrace{+ \log D_\psi}_{\text{additive difference}} + \log t, \tag{3.6}$$

as shown in figure 3.11. Coarse-graining must not modify physics, but speed up
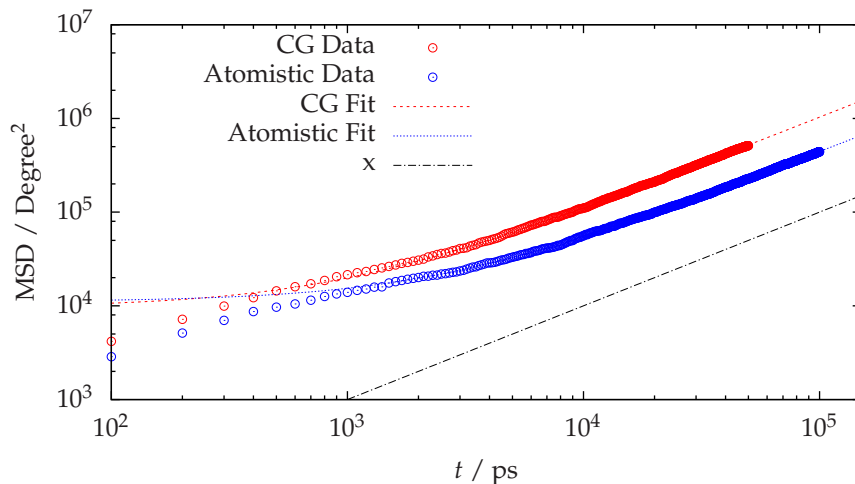
Figure 3.11: Log-log plot of the MSD. The plot shows one in one hundred data points.

simulation runs, i.e., in the long-time limit, both models should lead to the same diffusion. Rescaling the data obtained from the atomistic run according to

$$t \rightarrow t' = t/\zeta, \tag{3.7}$$

will lead to matched diffusive dynamics (for $t \rightarrow \infty$), shown in figure 3.12. However, the graphs deviate from each other for smaller times. Zooming into the region for times less than 1000 ps (figure 3.13), one notices an increasing gap for $t < 500$ ps, which corresponds to an MSD_ψ of approximately 15000 squared degrees.

If both angles are treated equally, we then obtain from equation (3.2)

$$\Delta \psi_i \approx 85°. \tag{3.8}$$

The increasing gap shows that – while the models produces a similar MSD for large times (after rescaling) – we observe different physics for small times. Coarse-graining polystyrene will fundamentally change short-time dynamics and is not suited, nor was it meant to be, for short simulation runs.

We will now try to predict at which particular angle $\Delta \psi_i$ we expect the comparison to brake down. The atomistic model uses a dihedral potential[20] in the form of (see
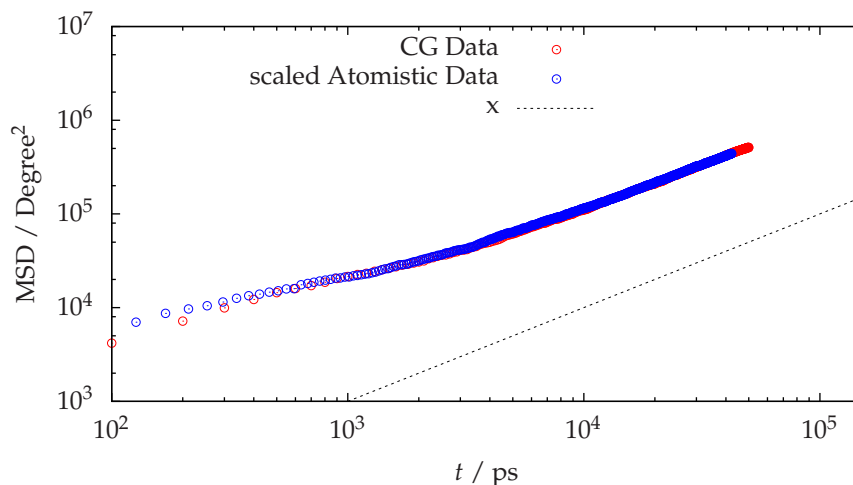
Figure 3.12: Log-log plot of the MSD after the atomistic data was rescaled using equation (3.7). This matches both MSD's for large t. The plot shows one in one hundred data points.

figure 3.15):

$$V(\psi_i) = 1 - \cos\left(3\left(\psi_i - \psi_{i,0}\right)\right),\tag{3.9}$$

where $\psi_{i,0} = 180°$ and *cis* corresponds to a dihedral angle of $0°$ (see figure 3.14(a)). Equation (3.9) gives not the true dihedral potential. If one takes the sidegroups and their non-bonded interactions into account, the potential looks less symmetric and its minima at $60°$ and $300°$ are shifted to higher energies. We neglect these additional terms in our discussion.

The potential in equation (3.9) implies that a particle will have to move fore more than $60°$ in order to escape from one minimum and cross the barrier. This marks the end of short-time dynamics and allows for diffusion, the crucial point for a CG model which aims at accelerating long-time dynamics.

The value of $60°$ is confirmed by simulation data, where we performed successful rescaling down to an angle of approximately $85°$.

Finally, we investigate both angles seperately. Table 3.4 sums up the results of figures 3.16 and 3.17. We expect the single angles to be the same, since the system under consideration is symmetric in both descriptions. In fact, we notice a small, about 5%, difference for the diffusion constants in the atomistic description. In the CG description, the angles are fully equivalent.
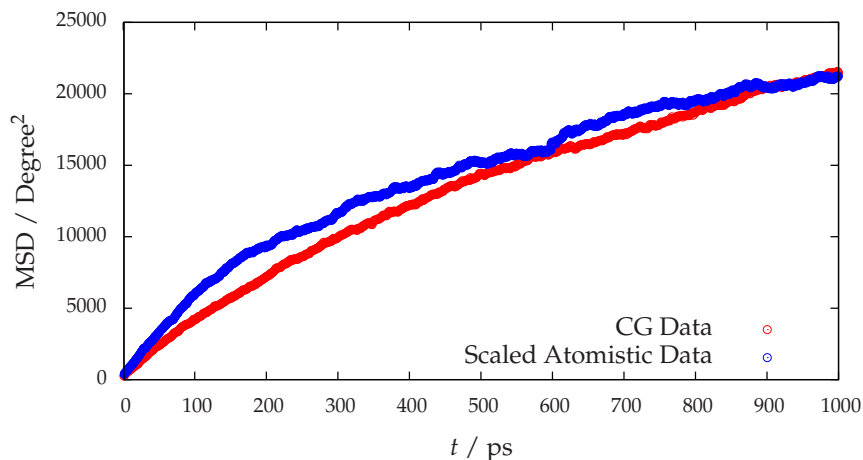
Figure 3.13: Regular MSD plot, zoomed into the region $0\,\mathrm{ps} < t < 1000\,\mathrm{ps}$. An increasing gap between the trajectories starts at $t \approx 500\,\mathrm{ps}$ and MSD ≈ 15000 squared degrees, respectively.

Direction	$\mathbf{D}^{\mathrm{cg}}$	$\mathbf{D}^{\mathrm{atom}}$	Scale Factor ζ
ψ_1	2.5557(2)	1.0567(2)	2.4119(5)
ψ_2	2.5562(2)	1.1040(1)	2.3153(4)

Table 3.4: Direction dependent diffusion coefficients of both models (in degree^2/ps). The scale factor ζ is calculated in analogy to equation (3.5) and is of unit 1.

(a) *cis* state   (b) *trans* state
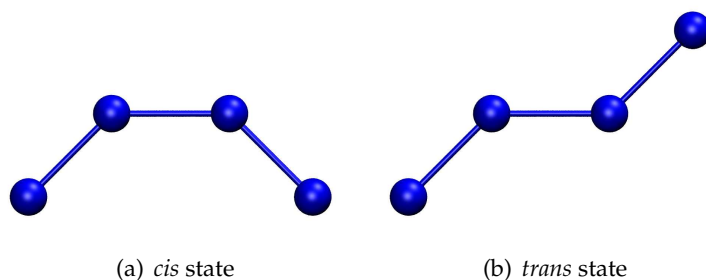
Figure 3.14: Two conventions in a molecule consisting of four atoms (or beads). Biochemistry uses the state shown in (a) to define the $0°$ dihedral angle, while the polymer world uses (b) as $0°$. In this thesis, *cis* is used as the default state in order to stay consistent with reference [20].
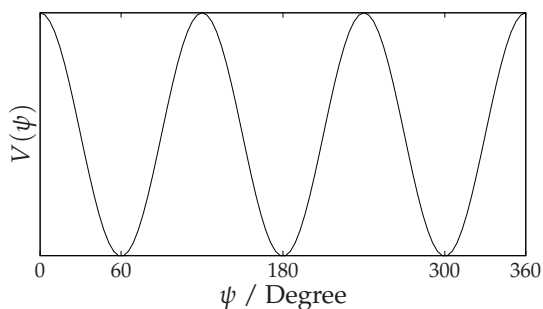
Figure 3.15: Schematic plot of the potential in equation (3.9). This plots corresponds to a simplified model where the influence of sidechains is neglected.

(a)

(b)

(c)

(d)
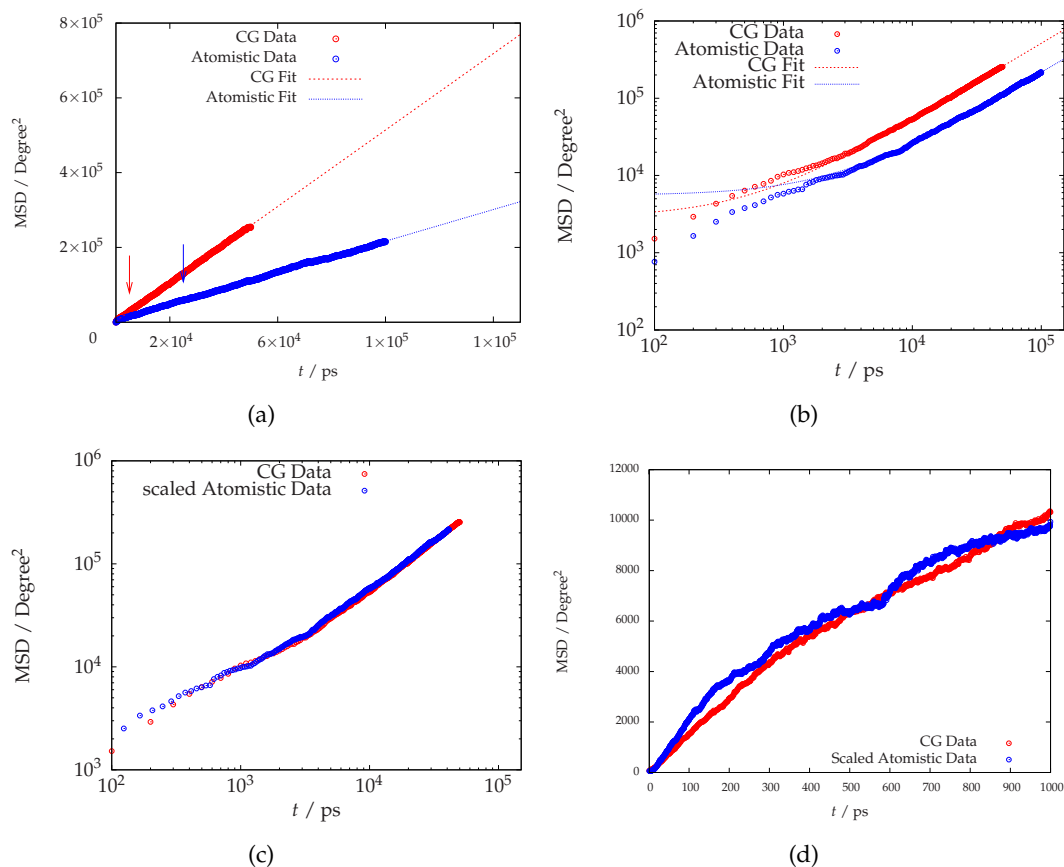
Figure 3.16: Regular (a) and log-log (b) plot of $(\Delta\psi_1)^2$. Log-log MSD plot (c) after time rescaling. (d) shows a smaller section.
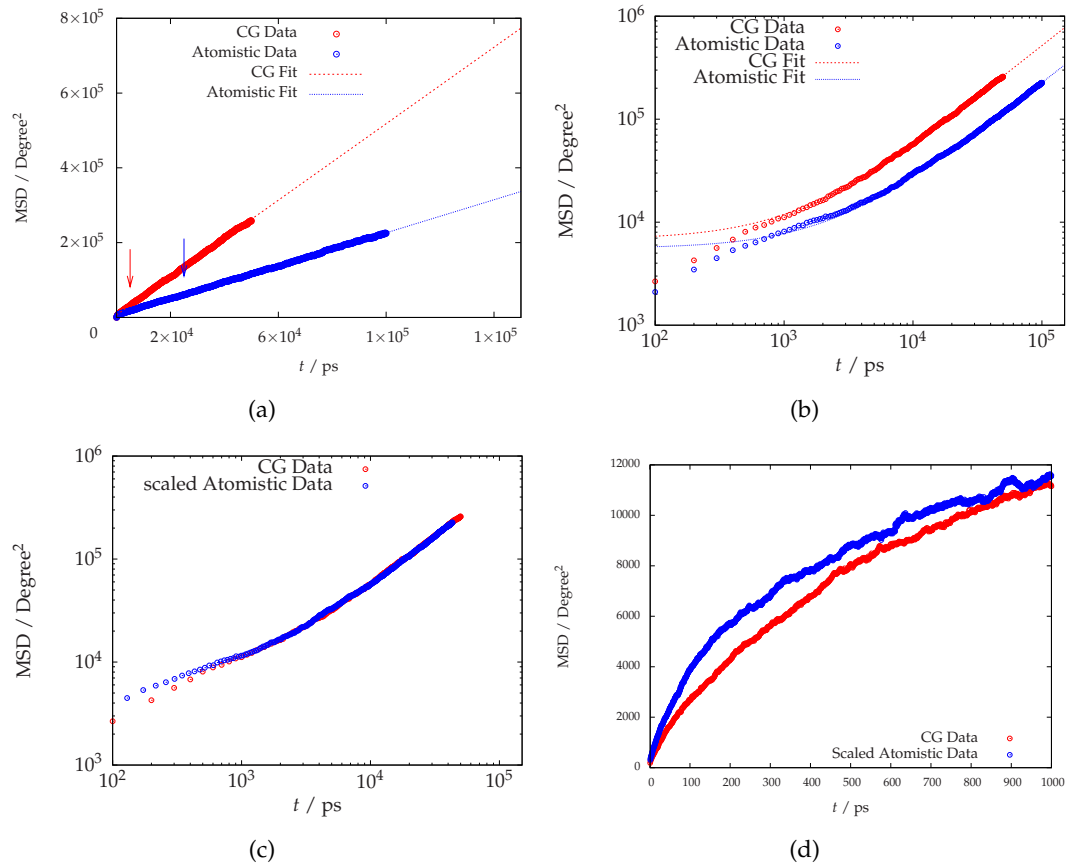
Figure 3.17: Regular (a) and log-log 3.17(b) plot of $(\Delta\psi_2)^2$. Log-log MSD plot (c) after time rescaling. (d) shows a smaller section.

Summary and Conclusion

The aim of this work was the investigation of the time scaling behavior of coarse-graining mappings. The chosen approach uses diffusive dynamics to characterize the time scale of a modeled system. Possibilites of an analytic description of the diffusion were shown in chapter 1. The corresponding Fokker-Planck equation can not be solved exactly for the general case. Nevertheless, the performed steps are also useful for further thoughts and limiting cases.

Kramers' rate theory uses a harmonic approximation of wells and barriers and offers therefore only limited application to more realistic systems. For the test-system ($U(x) = cos(x)$), Kramers' theory agrees with the simulation data as long as $k_B T \ll E_b$ holds. The agreement also depends on the friction constant. Due to the mentioned limited application concerning potential form and temperature range, studies beyond testing cases have not been carried out. However, it is in principle possible to split any potential into multiple wells-barriers-pairs and combine the single rate constants to a global one. To do this for a specific system however, is significantly beyond the scope of this work.

The Smoluchowski limit describes the system in the high friction limit. Besides the analytically evaluated integration, numerical integration allows one to apply equation (1.52) to any periodic potential. The Smoluchowski result for the mobility μ was confirmed by simulations and is very useful to test conceptual ideas.

The underlying, more general, theory based on the Fokker-Planck equation is suited to be solved semi-analytically. The tridiagonal system in equation (1.25) can be solved numerically up to a very high accuracy level. Also, it can be generalized to multi-dimensional problems[25]. Thus, calculations made for the Smoluchowski limit leading to equation (1.52) can also be generalized to a multi-dimensional case.

Hyper-MD, a method that aims at accelerating dynamics, was introduced in section 2.2 and tested in section 3.2. It was shown that its application is very limited, due to the complicated potentials of more realistic systems.

All these approaches are based on the knowledge of the potential energy surface. One therefore needs to extract this potential beforehand. The most naive approach was unsuccessful and showed clearly how complex the situation is. Especially for molecular liquids, which contain strongly fluctuating local concentrations, this will not be possible without a huge effort.

Finally, a minimal polystyrene model was simulated using the atomistic as well as the coarse-grained description. The stochastic dynamics simulations allowed us to

directly measure the angular diffusion of both dihedrals. A manual rescaling of the data was performed in order to test the general idea of an uniform time scaling. It was shown that the CG model modifies the original dynamics and a rescaling based on the diffusive dynamics (long-time limit) will not hold for the ballistic regime (short-time limit).

In conclusion, the investigation and, especially, prediction of the time-scaling behavior of coarse-graining mappings is a challenging task, since neither the calculation of diffusion constants is possible for the general case, nor are the potentials simple enough to be suited for various methods.

All presented approaches and methods offer plenty of space for improvements. However, the original goal is probably unreachable – no simple method will be able to predict the time scaling behavior. In most cases the more pragmatic approach as tested for of certain motions and the question, whether they can lead to estimates of contributions to specific processes.

A Algorithms

Integration Scheme for Molecular Dynamics: Velocity-Verlet

Newton

One can use the force $\mathbf{f}$ from Newton's equation of motion for a single particle with mass m and cartesian coordinates $\mathbf{r}$

$$\mathbf{f}(t) = m\ddot{\mathbf{r}}(t) \tag{A.1}$$

to rewrite the discretized trajectory

$$\begin{aligned}
\mathbf{r}(t + \Delta t) = \mathbf{r}(t) &+ \Delta t \dot{\mathbf{r}}(t) \\
&+ \frac{1}{2}\Delta t^2 \ddot{\mathbf{r}}(t) \\
&+ \frac{1}{6}\Delta t^3 \dddot{\mathbf{r}}(t) \\
&+ \mathcal{O}(\Delta t^4)
\end{aligned} \tag{A.2}$$

to

$$\mathbf{r}(t + \Delta t) = \mathbf{r}(t) + \Delta t \mathbf{v}(t) + \frac{\Delta t^2}{2m}\mathbf{f}(t) + \mathcal{O}(\Delta t^3) \tag{A.3}$$

and

$$\mathbf{v}(t + \Delta t) = \mathbf{v}(t) + \frac{\Delta t}{m}\mathbf{f}(t) + \frac{\Delta t^2}{2m}\dot{\mathbf{f}}(t) + \mathcal{O}(\Delta t^3). \tag{A.4}$$

Equations (A.3) and (A.4) are the scheme for the Euler algorithm. Since this algorithm neither preserves phase-space nor is time-reversible, we take the next step towards a more sophisticated algorithm. Adding and substracting

$$\mathbf{r}(t - \Delta t) = \mathbf{r}(t) - \Delta t \mathbf{v}(t) + \frac{\Delta t^2}{2m}\mathbf{f}(t) - \frac{1}{6}\Delta t^3 \dddot{\mathbf{r}}(t) + \mathcal{O}(\Delta t^4) \tag{A.5}$$

to and from equation (A.3) leads to

$$\mathbf{r}(t + \Delta t) = 2\mathbf{r}(t) - \mathbf{r}(t - \Delta t) + \frac{\Delta t^2}{m}\mathbf{f}(t) + \mathcal{O}(\Delta t^4) \tag{A.6}$$

and

$$\mathbf{v}(t) = \frac{\mathbf{r}(t + \Delta t) - \mathbf{r}(t - \Delta t)}{2\Delta t} + \mathcal{O}(\Delta t^2). \tag{A.7}$$

Finally, we use

$$\Delta t \dot{\mathbf{f}}(t) = \mathbf{f}(t + \Delta t) - \mathbf{f}(t) + \mathcal{O}(\Delta t^3) \tag{A.8}$$

to rewrite equation (A.4) and obtain the velocity Verlet algorithm

$$\mathbf{r}(t + \Delta t) = \mathbf{r}(t) + \Delta t \mathbf{v}(t) + \frac{\Delta t^2}{2m} \mathbf{f}(t) + \mathcal{O}(\Delta t^3),$$
$$\mathbf{v}(t + \Delta t) = \mathbf{v}(t) + \frac{\Delta t}{2m} [\mathbf{f}(t) + \mathbf{f}(t + \Delta t)] + \mathcal{O}(\Delta t^3). \tag{A.9}$$

We obtain the same result by solving Liouville's equation. Liouville's equation is the basis for deriving symplectic integrators.

Let $\mathbf{\Gamma}(t)$ be a trajectory in the phase-space $\mathbf{\Gamma} = \{\mathbf{r}, \mathbf{p}\}$ formed by all positions and momenta and let $\rho(\mathbf{r}, \mathbf{p})$ be the phase-space density. Using the Liouville operator $\mathcal{L}$

$$\mathcal{L} = i\mathcal{L}_{\mathbf{r}} + \mathcal{L}_{\mathbf{p}}, \tag{A.10}$$

$$= \dot{\mathbf{r}} \frac{\partial}{\partial \mathbf{r}} + \dot{\mathbf{p}} \frac{\partial}{\partial \mathbf{p}}. \tag{A.11}$$

consisting of a position and a momentum part we can formulate and formally integrate the equation of motion for one observable $A(\mathbf{\Gamma}; t)$,

$$\frac{\mathrm{d}}{\mathrm{d}t} A(\mathbf{\Gamma}; t) = i\mathcal{L} A(\mathbf{\Gamma}; t) \tag{A.12}$$

to obtain (omitting $\mathbf{\Gamma}$)

$$A(t + \Delta t) = e^{i\mathcal{L} \Delta t} A(t). \tag{A.13}$$

Trotter expanding the Liouville operator

$$e^{i(\mathcal{L}_{\mathbf{r}} + \mathcal{L}_{\mathbf{p}})\Delta t} = e^{i\frac{\Delta t}{2}\mathcal{L}_{\mathbf{p}}} e^{i\Delta t \mathcal{L}_{\mathbf{r}}} e^{i\frac{\Delta t}{2}\mathcal{L}_{\mathbf{p}}} + \mathcal{O}(\Delta t^3) \tag{A.14}$$

and subsequently applying these single factors to $\mathbf{r}$ or $\mathbf{p}$, respectivley, leads to equation (A.9). Since the operators $\mathcal{L}_{\mathbf{r}}$ and $\mathcal{L}_{\mathbf{p}}$ are hermitian, $e^{i\frac{\Delta t}{2}\mathcal{L}_{\mathbf{p}}} e^{i\Delta t \mathcal{L}_{\mathbf{r}}} e^{i\frac{\Delta t}{2}\mathcal{L}_{\mathbf{p}}}$ is unitary and implies phase-space preservation. Also, time-reversibility is satisfied since the equations are symmetric with respect to future and past coordinates.

Langevin

For the Langevin equation of motion

$$\dot{\mathbf{r}}(t) = \frac{1}{m}\mathbf{p}(t) \text{ and} \tag{A.15}$$

$$\dot{\mathbf{p}}(t) = \mathbf{F} - \gamma\frac{\mathbf{p}(t)}{m} + \mathbf{f}, \tag{A.16}$$

where $\mathbf{F}(\mathbf{r}) = -\nabla U(\mathbf{r})$ is the force derived from the Potential U, γ the friction constant (mass m included) and $\mathbf{f}$ the Gaussian white noise with

$$\langle \mathbf{f}(t) \rangle = 0, \tag{A.17}$$
$$\langle \mathbf{f}(t)\,\mathbf{f}(t') \rangle = 2\,\gamma k_B T\,\delta(t - t'). \tag{A.18}$$

We use the Fokker-Planck picture (Kramers-Moyal expansion, see reference [26])

$$\partial_t \rho(\mathbf{\Gamma}; t) = (\mathcal{L}_1 + \mathcal{L}_2 + \mathcal{L}_3 + \mathcal{L}_4)\,\rho(\mathbf{\Gamma}; t) \tag{A.19}$$

with

$$\mathcal{L}_1 = -\frac{\partial}{\partial \mathbf{r}} \cdot \frac{\mathbf{p}}{m}, \tag{A.20}$$

$$\mathcal{L}_2 = -\frac{\partial}{\partial \mathbf{p}} \cdot \mathbf{F}, \tag{A.21}$$

$$\mathcal{L}_3 = \gamma\frac{\partial}{\partial \mathbf{p}} \cdot \frac{\mathbf{p}}{m}, \tag{A.22}$$

$$\mathcal{L}_4 = k_B T\,\gamma\,\frac{\partial^2}{\partial \mathbf{p}^2}, \tag{A.23}$$

and again the Trotter expansion (note that only $\mathcal{L}_1$ has derivatives with respect to the position, whereas $\mathcal{L}_2 + \mathcal{L}_3 + \mathcal{L}_4$ differentiates with respect to the momentum)

$$
\begin{aligned}
&e^{(\mathcal{L}_1 + \mathcal{L}_2 + \mathcal{L}_3 + \mathcal{L}_4 +)\Delta t} \\
&= e^{\mathcal{L}_1 \frac{\Delta t}{2}} e^{(\mathcal{L}_2 + \mathcal{L}_3 + \mathcal{L}_4)\Delta t} e^{\mathcal{L}_1 \frac{\Delta t}{2}} + \mathcal{O}(\Delta t^3)
\end{aligned}
\tag{A.24}
$$

to derive an algorithm which subsequently shifts the position by $\frac{\Delta t}{2}$, the momentum by Δt and again the position by $\frac{\Delta t}{2}$. The only approximation we made is neglecting terms of the order of Δt^3 and higher. The solution for the equations of motion (obtained in analogy to equation (A.13)) can be found exactly from here on.

The position update is given by

$$\mathbf{r}(t + \frac{\Delta t}{2}) = \mathbf{r}(t) + \frac{\Delta t}{2}\frac{\mathbf{p}(t)}{m}. \tag{A.25}$$

The momentum update is given by solving the Langevin equation (A.16). The force **F** is constant during this step allowing us to find an exact solution.

Rewrite equation (A.16) to

$$\left(\frac{\mathrm{d}}{\mathrm{d}t} + \frac{\gamma}{m} \right) \mathbf{p} = \mathbf{F} + \mathbf{f}. \tag{A.26}$$

The homogenous case

$$\left(\frac{\mathrm{d}}{\mathrm{d}t} + \frac{\gamma}{m} \right) \mathbf{p} = 0 \tag{A.27}$$

is solved by

$$\mathbf{p}(t) = e^{-\frac{\gamma}{m}t} \mathbf{p}(0). \tag{A.28}$$

Variation of constants suggests the ansatz

$$\mathbf{p}(t) = e^{-\frac{\gamma}{m}t} \boldsymbol{\pi}(t) \tag{A.29}$$

which results in

$$\frac{\mathrm{d}}{\mathrm{d}t} \boldsymbol{\pi}(t) = e^{\frac{\gamma}{m}t} \left(\mathbf{F} + \mathbf{f}(t) \right). \tag{A.30}$$

Equation (A.30) for one timestep is solved by

$$\boldsymbol{\pi}(\Delta t) = \frac{m}{\gamma} \left(e^{\frac{\gamma}{m}\Delta t} - 1 \right) \mathbf{F} + \int_0^{\Delta t} \mathrm{d}t\, e^{\frac{\gamma}{m}t} \mathbf{f}(t) + \boldsymbol{\pi}(0) \tag{A.31}$$

$$\Leftrightarrow \quad \mathbf{p}(\Delta t) = e^{-\frac{\gamma}{m}\Delta t} \mathbf{p}(0) + \frac{m}{\gamma} \left(1 - e^{-\frac{\gamma}{m}\Delta t} \right) \mathbf{F} + \int_0^{\Delta t} \mathrm{d}t\, e^{-\frac{\gamma}{m}(\Delta t - t)} \mathbf{f}(t) \tag{A.32}$$

Since the RHS of equation (A.32) consists of constant terms and a white noise term, $\mathbf{p}(\Delta t)$ must be a Gaussian white noise variable, too. An explicit calculation for the

first two moments:

$$\langle \mathbf{p}(\Delta t) \rangle = e^{-\frac{\gamma}{m}\Delta t}\,\mathbf{p}(0) + \frac{m}{\gamma}\left(1 - e^{-\frac{\gamma}{m}\Delta t}\right)\,\mathbf{F}, \tag{A.33}$$

$$\left\langle \left(\mathbf{p}(\Delta t) - \langle \mathbf{p}(\Delta t) \rangle\right)^2 \right\rangle = \left\langle \left(\int_0^{\Delta t} \mathrm{d}t\, e^{-\frac{\gamma}{m}(\Delta t - t)}\mathbf{f}(t)\right)^2 \right\rangle$$

$$= \left\langle \int_0^{\Delta t} \mathrm{d}t\, e^{-\frac{\gamma}{m}(\Delta t - t)}\mathbf{f}(t) \cdot \int_0^{\Delta t} \mathrm{d}t'\, e^{-\frac{\gamma}{m}(\Delta t - t')}\mathbf{f}(t') \right\rangle$$

$$= 2\,\gamma k_B T \int_0^{\Delta t} \mathrm{d}t\, e^{-2\frac{\gamma}{m}(\Delta t - t)}$$

$$= m k_B T\left(1 - e^{-2\frac{\gamma}{m}\Delta t}\right), \tag{A.34}$$

where we used the fluctuation-dissipation relation. We can rewrite $\mathbf{p}(\Delta t)$ now to

$$\begin{aligned} \mathbf{p}(\Delta t) = \quad & e^{-\frac{\gamma}{m}\Delta t} \quad \mathbf{p}(0) \\ & + \frac{m}{\gamma}\left(1 - e^{-\frac{\gamma}{m}\Delta t}\right) \quad \mathbf{F} \\ & + \sqrt{m k_B T\left(1 - e^{-2\frac{\gamma}{m}\Delta t}\right)} \quad \boldsymbol{\xi}. \end{aligned} \tag{A.35}$$

The Gaussian white noise $\boldsymbol{\xi}$ has now unit variance. Taylor expanding equation (A.35) up to the order of one in Δt gives us the Euler algorithm of the update scheme. Thus, equation (A.35) is exact up to the order of two as a result of the Trotter expansion in equation (A.14) as stated above.

The three constant factors in equation (A.35) must be calculated only once at the beginning of the simulation.

```
lvvv_xfac = 0.5 * timestep / mass;
lvvv_d = exp(-lv_gamma / mass * timestep);
lvvv_q = mass / lv_gamma * (1.0 - lvvv_d);
lvvv_sigma = sqrt(mass * temperature * \
  (1.0 - exp(-2.0 * lv_gamma / mass * timestep)));
```

Listing A.1: Setting constant factors.

```
mdtime += timestep;
x += p*lvvv_xfac;
f = potentialIn.calcForce(x);
zeta = gsl_ran_gaussian(rng, 1.0);
p = p * lvvv_d + f * lvvv_q + zeta*lvvv_sigma;
x += p*lvvv_xfac;
```

Listing A.2: Integration of the equation of motion for one timestep.

Calculation of the Dihedral Angle

The dihedral angle as used in the context of this thesis is the angle between two planes and has a value between 0 and 2π. These planes are defined by four connected atoms or virtual sites.

Let ϕ be the angle between two planes with normal vectors $\mathbf{n_1}$ and $\mathbf{n_2}$. For the four given points $\mathbf{a_i}, i = 1 \dots 4$, in cartesian coordinates, we calculate their connecting vectors.

$$
\begin{aligned}
\mathbf{b_1} &= \mathbf{a_2} - \mathbf{a_1}, \\
\mathbf{b_2} &= \mathbf{a_3} - \mathbf{a_2}, \\
\mathbf{b_3} &= \mathbf{a_4} - \mathbf{a_3}.
\end{aligned}
\tag{A.36}
$$

The normal vectors are obtained by using the cross product,

$$
\mathbf{n_1} = \mathbf{b_1} \times \mathbf{b_2},
\tag{A.37}
$$

$$
\mathbf{n_2} = \mathbf{b_2} \times \mathbf{b_3}.
\tag{A.38}
$$

It is clear at this point, that we will need an inverse angle operation to obtain ϕ. In order to obtain a bijective mapping, we will make use of the atan2(ϕ) function that expects $\sin(\phi)$ and $\cos(\phi)$ as arguments and takes their sign into acccount to place the angle in the correct quadrant.

$$
\mathbf{n_1} \cdot \mathbf{n_2} = n_1 n_2 \cos(\phi) \quad \text{and}
\tag{A.39}
$$

$$
|\mathbf{n_1} \times \mathbf{n_2}| = n_1 n_2 \sin(\phi),
\tag{A.40}
$$

where $n_{1,2}$ is the length of $\mathbf{n_{1,2}}$. Equation (A.40) can be simplified as follows (Einstein summation convention)

$$\mathbf{n_1} \times \mathbf{n_2} = \mathbf{n_1} \times (\mathbf{b_2} \times \mathbf{b_3}) \tag{A.41}$$

$$= \varepsilon_{ijk}\, \mathrm{n}_1^i\, \varepsilon_{lmj}\, \mathrm{b}_2^l\, \mathrm{b}_3^m\, \mathbf{e^k} \tag{A.42}$$

$$= -\varepsilon_{ikj}\, \varepsilon_{lmj}\, \mathrm{n}_1^i\, \mathrm{b}_2^l\, \mathrm{b}_3^m\, \mathbf{e^k} \tag{A.43}$$

$$= -\left(\delta_{il}\, \delta_{km} - \delta_{im}\, \delta_{kl}\right) \mathrm{n}_1^i \mathrm{b}_2^l \mathrm{b}_3^m \mathbf{e^k} \tag{A.44}$$

$$= -\underbrace{(\mathbf{n_1} \cdot \mathbf{b_2})}_{=0} \mathbf{b_3} + (\mathbf{n_1} \cdot \mathbf{b_3})\, \mathbf{b_2} \tag{A.45}$$

$$= (\mathbf{n_1} \cdot \mathbf{b_3})\, \mathbf{b_2} \tag{A.46}$$

$$\Rightarrow \mathrm{n_1 n_2} \sin(\phi) = |(\mathbf{n_1} \cdot \mathbf{b_3})\, \mathbf{b_2}| \tag{A.47}$$

$$= (\mathbf{n_1} \cdot \mathbf{b_3})\, \mathbf{b_2} \frac{\mathbf{b_2}}{\mathrm{b_2}} \tag{A.48}$$

$$= (\mathbf{n_1} \cdot \mathbf{b_3})\, \mathrm{b_2} \tag{A.49}$$

$|\cdot|$ denotes the lenthg of the argument. The dihedral angle ϕ is then returned after calling $\mathrm{atan2}\left((\mathbf{n_1} \cdot \mathbf{b_3})\, \mathrm{b_2}, \mathbf{n_1} \cdot \mathbf{n_2}\right)$.

B Extracting the Dihedral Potential Energy Surface of Polystyrene

This section describes the method used for the extraction of the potential in section 3.3.

1. We start the procedure from the minimum configuration at ($\psi_1 = 150°$, $\psi_2 = 85°$).

2. ψ_2 is incremented by 5° and both dihedral angles are restrained to their values using a spring potential, $V_{restr} \propto (\psi_i - \psi_{i,0})^2$.

3. A MD simulation drives the system into the next local minimum. The resulting configuration is saved and used for the next iteration. The minimum energy is extracted.

4. Steps 2 and 3 are repeated until ψ_2 reaches 85° again. At 360°, ψ_2 is mapped back to 0°.

5. ψ_1 is now incremented by 5° and steps 2 - 4 are repeated until ψ_1 reaches 150° again. At 360°, ψ_1 is mapped back to 0°.

This is the most naive approach and leads to the following problems in systems with more than a few degrees of freedom[1]: The energy minimization depends on the initial configuration. E.g., rotating backward and forward, respectively, leads to different (local) minima. Also, the resulting potential is not 2π-periodic and thereby contradicts physics. This behavior is highly unwanted and makes the extraction of one meaningful potential impossible.

In a MD simulation, local minima prevent the system to overcome even the smallest barriers in order to find more favorable minima surrounding the desired configuration at (ψ_1, $\psi_2 + 5°$). Thus, a stochastic term was added to the MD simulation to enable to system to fully relax. Instead of the potential energy surface, the free energy surface (FES) was extracted. It is shown in figure 2.1 and offers only a small improvement. This means that higher energies are needed to overcome local barriers.

---

[1]E.g., for the CG dihedral PES, the method works well. However, it fails for the atomistic dihedral PES.

Thus, one needs to consider other methods for the purpose of finding a unique PES/FES. A quick study using simulated annealing and replica exchange[27], respectively, and temperatures up to 700K did still not lead to a FES that does not depend on the initial configuration.

A future analyis should use random initial configurations and – after applying dihedral restraints – slowly force the system into the desired configuration.

(a) Atomistic FES, T=10K

(b) Coarse-Grained FES, T=10K

(c) Atomistic FES, T=50K

(d) Coarse-Grained FES, T=50K
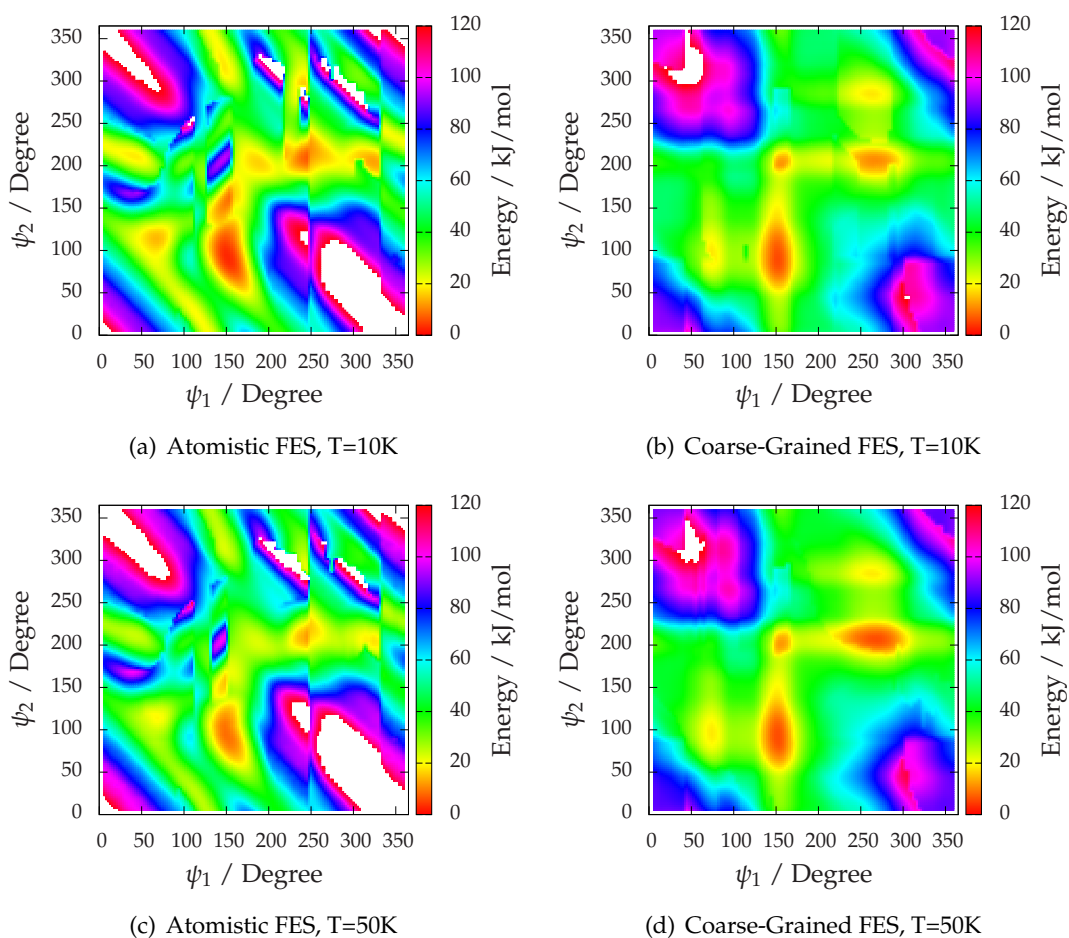
Figure 2.1: The free energy surface for the atomistic and the coarse-grained description. Obtained using a SD simulation at two different temperatures. Energy values in units of kJ/mol. Regions with energies above 120 kJ/mol appear white.

C Sample Gromacs .mdp File

A sample .mdp file as used in section 3.4 follows.

```
title                     = PS
cpp                       = /usr/bin/cpp
integrator                = sd
tinit                     = 0.0
dt                        = 0.001
nsteps                    = 100000000
init_step                 = 0
comm-mode                 = Angular
nstcomm                   = 1000
ld-seed                   = -1
emtol                     = 10
emstep                    = 0.01
niter                     = 20
fcstep                    = 0
nstcgsteep                = 1000
nbfgscorr                 = 10
nstxout                   = 10
nstvout                   = 0
nstfout                   = 0
nstcheckpoint             = 1000000
nstlog                    = 0
nstenergy                 = 0
nstxtcout                 = 0
xtc_precision             = 2000
xtc-grps                  =
energygrps                = system
nstlist                   = 0
ns_type                   = simple
pbc                       = no
rlist                     = 1.5
domain-decomposition      = no
coulomb_type              = cut-off
rcoulomb_switch           = 0
rcoulomb                  = 1.5
epsilon_r                 = 1.0
vdw_type                  = Cut-off
rvdw_switch               = 0
rvdw                      = 1.5
DispCorr                  = No
table-extension           = 1
```

```
fourierspacing          = 0.12
pme_order               = 4
ewald_rtol              = 1e−05
ewald_geometry          = 3d
epsilon_surface         = 0
optimize_fft            = no
gb_algorithm            = Still
nstgbradii              = 1
rgbradii                = 2
gb_saltconc             = 0
implicit_solvent        = No
tcoupl                  = v−rescale
tc−grps                 = system
tau_t                   = 0.01
ref_t                   = 503
Pcoupl                  = no
tau_p                   = 2.0
compressibility         = 2.755e−5
ref_p                   = 1.01325
```

Listing C.1: Sample .mdp file as used in section 3.4.

D Numerical Data

<table>
<tr><td colspan="5" align="center">(a) $\gamma = 0.1$</td></tr>
<tr><td>T</td><td>$\gamma\mu$</td><td>$\Delta\gamma\mu$</td><td>Kramers</td><td>Smoluchowski</td></tr>
<tr><td>0.10</td><td>0.0000</td><td>0.0000</td><td>0.0000</td><td>0.0000</td></tr>
<tr><td>0.14</td><td>0.0000</td><td>0.0000</td><td>0.0000</td><td>0.0000</td></tr>
<tr><td>0.18</td><td>0.0001</td><td>0.0000</td><td>0.0000</td><td>0.0005</td></tr>
<tr><td>0.20</td><td>0.0002</td><td>0.0000</td><td>0.0001</td><td>0.0013</td></tr>
<tr><td>0.22</td><td>0.0004</td><td>0.0000</td><td>0.0003</td><td>0.0030</td></tr>
<tr><td>0.26</td><td>0.0016</td><td>0.0000</td><td>0.0010</td><td>0.0102</td></tr>
<tr><td>0.30</td><td>0.0041</td><td>0.0000</td><td>0.0025</td><td>0.0243</td></tr>
<tr><td>0.34</td><td>0.0084</td><td>0.0001</td><td>0.0049</td><td>0.0462</td></tr>
<tr><td>0.38</td><td>0.0142</td><td>0.0000</td><td>0.0081</td><td>0.0754</td></tr>
<tr><td>0.40</td><td>0.0189</td><td>0.0004</td><td>0.0101</td><td>0.0924</td></tr>
<tr><td>0.42</td><td>0.0217</td><td>0.0003</td><td>0.0122</td><td>0.1107</td></tr>
<tr><td>0.46</td><td>0.0315</td><td>0.0008</td><td>0.0168</td><td>0.1503</td></tr>
<tr><td>0.50</td><td>0.0437</td><td>0.0011</td><td>0.0219</td><td>0.1924</td></tr>
</table>

<table>
<tr><td colspan="5" align="center">(b) $\gamma = 0.2$</td></tr>
<tr><td>T</td><td>$\gamma\mu$</td><td>$\Delta\gamma\mu$</td><td>Kramers</td><td>Smoluchowski</td></tr>
<tr><td>0.10</td><td>0.0000</td><td>0.0000</td><td>0.0000</td><td>0.0000</td></tr>
<tr><td>0.14</td><td>0.0000</td><td>0.0000</td><td>0.0000</td><td>0.0000</td></tr>
<tr><td>0.18</td><td>0.0001</td><td>0.0000</td><td>0.0001</td><td>0.0005</td></tr>
<tr><td>0.20</td><td>0.0003</td><td>0.0000</td><td>0.0003</td><td>0.0013</td></tr>
<tr><td>0.22</td><td>0.0006</td><td>0.0000</td><td>0.0006</td><td>0.0030</td></tr>
<tr><td>0.26</td><td>0.0023</td><td>0.0000</td><td>0.0020</td><td>0.0102</td></tr>
<tr><td>0.30</td><td>0.0056</td><td>0.0000</td><td>0.0048</td><td>0.0243</td></tr>
<tr><td>0.34</td><td>0.0112</td><td>0.0002</td><td>0.0093</td><td>0.0462</td></tr>
<tr><td>0.38</td><td>0.0186</td><td>0.0002</td><td>0.0155</td><td>0.0754</td></tr>
<tr><td>0.40</td><td>0.0240</td><td>0.0000</td><td>0.0192</td><td>0.0924</td></tr>
<tr><td>0.42</td><td>0.0295</td><td>0.0001</td><td>0.0231</td><td>0.1107</td></tr>
<tr><td>0.46</td><td>0.0423</td><td>0.0001</td><td>0.0320</td><td>0.1503</td></tr>
<tr><td>0.50</td><td>0.0568</td><td>0.0008</td><td>0.0417</td><td>0.1924</td></tr>
</table>

<table>
<tr><td colspan="5" align="center">(c) $\gamma = 0.5$</td></tr>
<tr><td>T</td><td>$\gamma\mu$</td><td>$\Delta\gamma\mu$</td><td>Kramers</td><td>Smoluchowski</td></tr>
<tr><td>0.10</td><td>0.0000</td><td>0.0000</td><td>0.0000</td><td>0.0000</td></tr>
<tr><td>0.14</td><td>0.0000</td><td>0.0000</td><td>0.0000</td><td>0.0000</td></tr>
<tr><td>0.18</td><td>0.0002</td><td>0.0000</td><td>0.0002</td><td>0.0005</td></tr>
<tr><td>0.20</td><td>0.0005</td><td>0.0000</td><td>0.0006</td><td>0.0013</td></tr>
<tr><td>0.22</td><td>0.0012</td><td>0.0000</td><td>0.0013</td><td>0.0030</td></tr>
<tr><td>0.26</td><td>0.0044</td><td>0.0000</td><td>0.0043</td><td>0.0102</td></tr>
<tr><td>0.30</td><td>0.0105</td><td>0.0000</td><td>0.0104</td><td>0.0243</td></tr>
<tr><td>0.34</td><td>0.0203</td><td>0.0000</td><td>0.0201</td><td>0.0462</td></tr>
<tr><td>0.38</td><td>0.0328</td><td>0.0003</td><td>0.0334</td><td>0.0754</td></tr>
<tr><td>0.40</td><td>0.0403</td><td>0.0004</td><td>0.0413</td><td>0.0924</td></tr>
<tr><td>0.42</td><td>0.0484</td><td>0.0007</td><td>0.0499</td><td>0.1107</td></tr>
<tr><td>0.46</td><td>0.0675</td><td>0.0002</td><td>0.0690</td><td>0.1503</td></tr>
<tr><td>0.50</td><td>0.0885</td><td>0.0004</td><td>0.0899</td><td>0.1924</td></tr>
</table>

<table>
<tr><td colspan="5" align="center">(d) $\gamma = 1.0$</td></tr>
<tr><td>T</td><td>$\gamma\mu$</td><td>$\Delta\gamma\mu$</td><td>Kramers</td><td>Smoluchowski</td></tr>
<tr><td>0.10</td><td>0.0000</td><td>0.0000</td><td>0.0000</td><td>0.0000</td></tr>
<tr><td>0.14</td><td>0.0000</td><td>0.0000</td><td>0.0000</td><td>0.0000</td></tr>
<tr><td>0.18</td><td>0.0003</td><td>0.0000</td><td>0.0003</td><td>0.0005</td></tr>
<tr><td>0.20</td><td>0.0009</td><td>0.0000</td><td>0.0009</td><td>0.0013</td></tr>
<tr><td>0.22</td><td>0.0020</td><td>0.0000</td><td>0.0020</td><td>0.0030</td></tr>
<tr><td>0.26</td><td>0.0070</td><td>0.0001</td><td>0.0068</td><td>0.0102</td></tr>
<tr><td>0.30</td><td>0.0155</td><td>0.0004</td><td>0.0165</td><td>0.0243</td></tr>
<tr><td>0.34</td><td>0.0299</td><td>0.0003</td><td>0.0318</td><td>0.0462</td></tr>
<tr><td>0.38</td><td>0.0495</td><td>0.0005</td><td>0.0529</td><td>0.0754</td></tr>
<tr><td>0.40</td><td>0.0610</td><td>0.0001</td><td>0.0654</td><td>0.0924</td></tr>
<tr><td>0.42</td><td>0.0725</td><td>0.0006</td><td>0.0790</td><td>0.1107</td></tr>
<tr><td>0.46</td><td>0.1025</td><td>0.0004</td><td>0.1092</td><td>0.1503</td></tr>
<tr><td>0.50</td><td>0.1328</td><td>0.0002</td><td>0.1422</td><td>0.1924</td></tr>
</table>

Table D.1: Numerical data of figure 3.2. Part one of two.

| | (a) $\gamma = 2.0$ | | | | | (b) $\gamma = 5.0$ | | | |
T	$\gamma\mu$	$\Delta\gamma\mu$	Kramers	Smoluchowski	T	$\gamma\mu$	$\Delta\gamma\mu$	Kramers	Smoluchowski
0.10	0.0000	0.0000	0.0000	0.0000	0.10	0.0000	0.0000	0.0000	0.0000
0.14	0.0000	0.0000	0.0000	0.0000	0.14	0.0001	0.0000	0.0000	0.0000
0.18	0.0005	0.0000	0.0004	0.0005	0.18	0.0006	0.0000	0.0005	0.0005
0.20	0.0012	0.0000	0.0012	0.0013	0.20	0.0015	0.0000	0.0014	0.0013
0.22	0.0026	0.0000	0.0027	0.0030	0.22	0.0029	0.0000	0.0031	0.0030
0.26	0.0093	0.0002	0.0091	0.0102	0.30	0.0242	0.0000	0.0257	0.0243
0.30	0.0211	0.0002	0.0221	0.0243	0.30	0.0242	0.0000	0.0257	0.0243
0.34	0.0389	0.0004	0.0427	0.0462	0.34	0.0446	0.0005	0.0496	0.0462
0.38	0.0643	0.0003	0.0709	0.0754	0.38	0.0735	0.0010	0.0825	0.0754
0.40	0.0804	0.0004	0.0877	0.0924	0.40	0.0913	0.0004	0.1019	0.0924
0.42	0.0961	0.0007	0.1060	0.1107	0.42	0.1090	0.0011	0.1232	0.1107
0.46	0.1350	0.0008	0.1464	0.1503	0.46	0.1518	0.0013	0.1701	0.1503
0.50	0.1741	0.0014	0.1907	0.1924	0.50	0.1946	0.0035	0.2216	0.1924

Table D.2: Numerical data of figure 3.2. Part two of two.

E List of Abbreviations and Remarks

List of used abbreviations

CG	Coarse-graining / coarse-grained
MD	Molecular dynamics
SD	Stochastic dynamics
MSD	Mean square displacement
TST	Transition state theory
FPE	Fokker-Planck equation
PES	Potential energy surface
FES	Free energy surface

Mathematica's Fitting Routine

The Mathematica function `NonlinearRegress[]` (least-squares fit) was used for all fits. The `Standard Error` from the `ParameterCITable` was taken as the fitting error.

Plots

All plots have been created using Gnuplot 4.5.
The visualization of molecular structures were created with Visual Molecular Dynamics 1.8.6 (VMD) and the ray tracing system Tachyon 0.98.
Chemicals schemes were drawn using MSketch 5.0.

Source and Data

This document, source codes and data – unless its size exceeds the capacatiy of a DVD – can be found on the disc attached to the back cover.

Bibliography

[1] O. Guvench and A. D. MacKerell Jr. *Comparison of protein force fields for molecular dynamics simulations*. Humana Press, 2008.

[2] D. Fritz, V. A. Harmandaris, K. Kremer, and N. F. A. van der Vegt. Coarse-grained polymer melts based on isolated atomistic chains: Simulation of polystyrene of different tacticities. *Macromolecules*, 42(19):7579 – 7588, 2009.

[3] H. Risken. *The Fokker-Planck Equation*. Springer Series in Synergetics. Springer, 2nd edition, 1996.

[4] D. Frenkel and B. Smit. *Understanding Molecular Simulation: From Algorithms to Applications*. Academic Press, 2nd edition, 2001.

[5] H. A. Kramers. Brownian motion in a field of force and the diffusion model of chemical reactions. *Physica*, 7(4):284 – 304, 1940.

[6] P. Hänggi, P. Talkner, and M. Borkovec. Reaction-rate theory: Fifty years after Kramers. *Reviews of Modern Physics*, 62(2):251 – 341, 1990.

[7] A. F. Voter. A method for accelerating the molecular dynamics simulation of infrequent events. *Journal of Chemical Physics*, 106(11):4665 – 4677, 1997.

[8] A. F. Voter. Hyperdynamics: Accelerated molecular dynamics of infrequent events. *Physical Review Letters*, 78(20):3908 – 3911, 1997.

[9] C. F. Sanz-Navarro and R. Smith. Numerical calculations using the hyper-molecular dynamics simulation method. *Computer Physics Communications*, 137 (1):206 – 221, 2001.

[10] X. G. Gong and J. W. Wilkins. Hyper molecular dynamics with a local bias potential. *Physical Review B*, 59(1):54 – 57, 1999.

[11] M. M. Steiner, P. A. Genilloud, and J. W. Wilkins. Simple bias potential for boosting molecular dynamics with the hyperdynamics scheme. *Physical Review B*, 57 (17):10236 – 10239, 1998.

[12] S. Pal and K. A. Fichthorn. Accelerated molecular dynamics of infrequent events. *Chemical Engineering Journal*, 74(1-2):77 – 83, 1999.

[13] J. C. Wang, S. Pal, and K. A. Fichthorn. Accelerated molecular dynamics of rare events using the local boost method. *Physical Review B*, 63(8), 2001.

[14] D. Hamelberg, J. Mongan, and J. A. McCammon. Accelerated molecular dynamics: A promising and efficient simulation method for biomolecules. *Journal of Chemical Physics*, 120(24):11919 – 11929, 2004.

[15] W. G. Rudd and A. F. Voter. Bias potentials for hyperdynamics simulations. 538: 485 – 490, 1999. Symposium on Multiscale Modelling of Materials, at the 1998 MRS Fall Meeting, Boston.

[16] A. Laio and M. Parrinello. Escaping free-energy minima. *Proceedings of the National Academy of Sciences of the United States of America*, 99(20):12562 – 12566, 2002.

[17] K. Kremer and F. Müller-Plathe. Multiscale problems in polymer science: Simulation approaches. *MRS Bulletin*, 26(3):205–210, 2001.

[18] C. Peter and K. Kremer. Multiscale simulation of soft matter systems. *Faraday Discussions*, 144:9 – 24, 2010.

[19] V. Rühle, C. Junghans, A. Lukyanov, K. Kremer, and D. Andrienko. Versatile object-oriented toolkit for coarse-graining applications. *Journal of Chemical Theory and Computation*, 2009.

[20] F. Müller-Plathe. Local structure and dynamics in solvent-swollen polymers. *Macromolecules*, 29(13):4782 – 4791, 1996.

[21] V. A. Harmandaris, D. Reith, N. F. A. Van der Vegt, and K. Kremer. Comparison between coarse-graining models for polymer systems: Two mapping schemes for polystyrene. *Macromolecular Chemistry and Physics*, 208(19-20):2109 – 2120, 2007.

[22] H. J. Limbach, A. Arnold, B. A. Mann, and C. Holm. ESPResSo - an extensible simulation package for research on soft matter systems. *Computer Physics Communications*, 174(9):704 – 727, 2006.

[23] *Mathematica*. Wolfram Research, Inc., Champaign, Illinois, version 7.0 edition, 2008.

[24] B. Hess, C. Kutzner, D. van der Spoel, and E. Lindahl. Gromacs 4: Algorithms for highly efficient, load-balanced, and scalable molecular simulation. *Journal of Chemical Theory and Computation*, 4(3):435 – 447, 2008.

[25] H. Risken and H. D. Vollmer. Brownian motion in periodic potentials; nonlinear response to an external force. *Zeitschrift für Physik B Condensed Matter*, 33(3):297 – 305, 1979.

[26] B. Dünweg. Langevin methods. In *Computer Simulations of Surfaces and Interfaces*, volume 114 of *Nato Science Series, Series II: Mathematics, Physics and Chemistry*, pages 77 – 92. Springer, 2003.

[27] Koji Hukushima and Koji Nemoto. Exchange monte carlo method and application to spin glass simulations. *Journal of the Physical Society of Japan*, 65(6): 1604–1608, 1996.